Journal of Dynamics of Fluids

Volume No. 13

Issue No. 1

January - April 2025

ENRICHED PUBLICATIONS PVT.LTD

JE - 18,Gupta Colony, Khirki Extn,
Malviya Nagar, New Delhi - 110017.
E- Mail: info@enrichedpublication.com
Phone :- +91-8877340707

Journal of Dynamics of Fluids

Aims and Scope

Journal of Dynamics of fluids is an scientific journal that publishes articles, research notes, debate and short reports in all areas of Fluid Dynamics.

Subject areas suitable for publication include, but are not limited to the following fields:

- Aeroacoustics
- Bluff Body Flows
- Bubbles and Droplets
- Dynamics of Dispersed Particles
- Fluid-structure Interactions
- Flow Stability and Transition to Chaos
- Flow Control Methods
- Gravitational Convection Solidification

Journal of Dynamics of Fluids

Journal of Dynamics of Fluids

(Volume No. 13, Issue No. 1, January - April 2025)

Contents

Performance Assessment of a Nearshore DistensibleTube Wave Attenuator at Model Scale

Antonio C. Mendes1 and Francisco P. Braga2
Laboratory of Fluid Mechanics and Turbomachinery
Electromechanical Engineering Department
Universidade da Beira Interior, 6201-001 Covilha, Portugal

A B S T R A C T

A water-filled floating rubber tube is considered for ocean wave powerabsorption. Its working principle relies on wave-excited pressure bulgesdelivered by the tube into a forward-bent oscillating water column at its stern.The present study reports on wave flume tests conducted with a 1:70 scale model of this system, in deep and intermediate regular waves having small and finite amplitudes. An orifice-flow pneumatic power take-off is used to emulate an air turbine generator set. Assuming incompressible flow, its nonlinear pressure to volume-flow characteristic is here obtained from the water column free-surface measurements, for different wave loading conditions. Two situations are considered: the system operating over a sloping bottom nearshore or fitted into a sea-wall onshore. In this latter case the influence of water depth variation is also investigated. The hydrodynamic and overall efficiencies of the system are provided. It is demonstrated that the system is very efficient when the tube is allowed to operate with three degrees-offreedom: in bending, surging and bulging modes. Additionally, it is shown that its performance is higher in the onshore configuration.

Keywords: Wave energy; Distensible tube; Wave-flume tests; Performance assessment.

1. Introduction

Estimates of the global gross wave energy potential advanced by the World Energy Council in 2016 [1] point to 32 000 *h* per year. However, it is generally assumed that the gross nearshore resource is much smaller than the corresponding gross wave energy potential offshore, regardless of bathymetry. This is not always so, as the wave attenuation will be closely dependent on the continental shelf and the directionality of the waves. Sometimes there can even be a natural focussing effect that may be beneficial for wave energy harnessing. Apropos, Foley and Whittaker [2] argue that the gross wave power resource is not an appropriate measure. Instead they have introduced a rational quantification of the nearshore exploitable wave energy resource, which accounts for wave directionality and also for the rated power limit of the plant. From this point of view the wave energy resource will not be so dramatically reduced by refraction near the coast, because the directional spread of the waves tends to become smaller at the nearshore. In fact, for the typical wave climates of the mid and north Atlantic the reduction of net wave power density is expected to be well below 20% in seabed slopes of 1:100. If we accept this definition, the deployment of wave energy converters in the nearshore may become economically viable.

The purpose of the present research is to use a concept proposed by Farley and Rainey in 2006 [3] and adapt it to operate in the nearshore. It consists of a long floating rubber tube filled with water – The Anaconda – that can be utilized to efficiently harness the energy of ocean waves. An independent analysis done by the Carbon Trust in 2010 suggested that this concept had the potential to deliver significant reductions in the cost of wave energy. It could therefore belong to a future generation of profitable ocean renewable energy converters. The first laboratory tests of the Anaconda were carried out in 2007, with a model of this device having a 2.5m long latex tube, 0.078m in diameter and 0.15m wall thickness [4]. The model was tested in a wave flume, submerged just below the still water level. The experiment provided evidence of a capture-width of 3 to 4 tube diameters in a wide range of incident wave frequencies. Since the device was not fitted with any power take-off system, the wave energy it absorbed was in this case accounted for by hysteresis losses in the rubber and friction losses of the internal flow. The working principle of the Anaconda wave power converter has been reanalysed and discussed in detail in [5]. Later, Chaplin et al. [6] performed in 2010 a second series of tests with a 1:25 scale model at the Offshore Wave Basin of the Danish Hydraulic Institute, in Denmark. This time the tests were carried out with a 7m long rubber tube, having a diameter of 0.215m and 1 to 2mm wall thickness. They were essentially concerned with the measurement of the waves radiated by the tube. Following an extensive series of experiments carried out at Solent University wave tank in Southampton, [7] reports on a linear pneumatic power take-off of adjustable impedance. These tests involved a 1:25 scale model comprising a 7m long tube, made out of rubber and fabric, with 0.25m in diameter and held fixed at either end. For the first time, theoretical predictions of power capture were found to be in close agreement with measurements.

Aiming to assess the Anaconda performance under intermediate regular waves, in 2014 a 1:100 scale distensible tube model has been coupled at its stern with a forward-bent oscillating water column (OWC) and tested in a wave flume [8]. In this case the 0.81m long latex tube having a diameter of 7.8 mm floated freely and the OWC model was assembled to a bottom-standing pillar. The pneumatic power take-off used in this experiment had a non-linear pressure to volume flow characteristic that adequately represented an impulse air turbine. The results of thisstudy shed light on various aspects of the system's response to intermediate water waves and put in evidence the advantages of coupling a distensible tube with an OWC. In this context, a helpful discussion about the problem of a single circular OWC in linear theory is given in [9].The authors demonstrate that the commercial viability of circular vertical OWCs would require highly efficient power take-off systems; furthermore, in order to have a system capable of harnessing the energy of a large wave front, while delivering a reasonable air flow to the turbine, its optimal capture-width would have to be improved. In light of this the use of a forward-bent duct assembled to a distensible-tube, combined with the use of a reflecting wall, could help to achieve this goal.

The present study reports on experimental tests recently conducted with a 1:70 scale physical model of the OWC-connected distensible tube in a wave flume. The prototype is envisaged to make use of a 60m long rubber tube, having a diameter of about 7m, operating in water depths of 23m. The periods of the waves generated in the flume scale to 5 − 15m wave period and up to 5m maximum wave height, in full-scale. Two situations are modelled: the system operating over a sloping bottom nearshore, or fitted into a reflecting wall onshore. In this later case the system is tested both at constant depth or over the sloped bottom. The dynamic response of the system is obtained from the water column free-surface displacement measurements, in terms of its amplification factor. The air volume-flow across the power take-off is determined by applying Bernoulli's law for incompressible flow, thereafter yielding the extracted power. The energy capture efficiency of the system is then obtained under the form of a capturewidth expressed in tube diameters. It is demonstrated that the system is very efficient when allowed to operate with three degrees-of-freedom: in bending, surging and bulging modes. Additionally, it is shown that its performance may be improved by incorporating the proposed onshore configuration.

2. The physical model

A physical model of the OWC-connected distensible tube has been built and tested in a wave flume at a scale of approximately 1:70. The 8m long and 0.3m wide flume is equipped with a paddle-type wavemaker and a sloping beach 1.28m in length at the opposite end. The water depth in the flume is h = 0.33m. The 0.904m long tube is made out of 0.16mm thick latex, and its bow is closed by a wood nose floating head to waves. At its stern the tube is connected to an acrylic vertical circular duct of radius cm = 3.61 cm, at a depth of 1.9 cm, through a partially submerged PVC elbow. The nose of the tube is itself connected to a water feeding system by means of a 2.5mm diameter plastic hose, with a tap that pierces the nose. A self-priming reversible flow water pump is used, enabling not only to inflate but also to deflate the rubber tube. The pump can deliver a volume flow of 0.6l/mm. By properly adjusting the water head $h0$ inside the duct just a few centimetres above the still-water level outside, the rubber tube can bepressurised at will and therefore conveniently tuned to the incident waves. In the present case it is set to $h0$ = 10 cm which results in a pressurized tube diameter d = 9.78 cm. A loose mooring system is also attached to the nose of the tube. The pneumatic power take-off (PTO) consists of an air chamber of height $h1$ = 57.5cm that connects to the atmosphere through a sharp-edged orifice plate of diameter d0. The pressure in the chamber builds under the action of the water piston inside the duct, forcing the air in and out through the orifice. Several calibrated orifices have been tested, with diameters ranging from d0 = 5.4mm to 17.2mm. The model was first tested in the nearshore configuration of Fig. 1, over a 30.1% sloped bottom. Afterwards it was tested on a reflecting wall over constant depth and over the sloping bottom. In Tables 1 and 2 the relevant dimensions of the physical model and PTO system are presented.

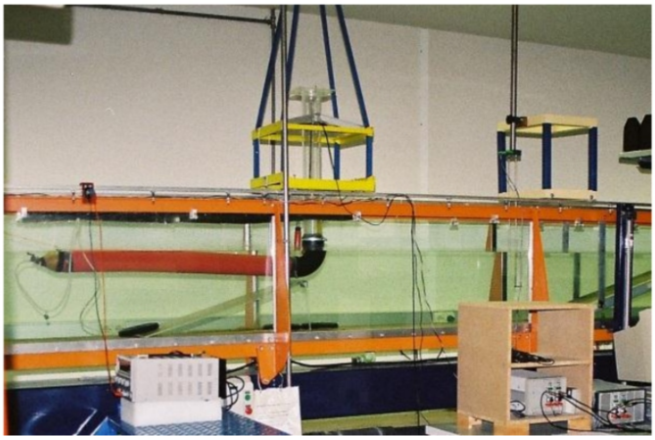

Figure 1: Distensible-tube wave attenuator over a sloping bottom in the wave-flume.

Table 1: Dimensions of the distensible tube at model scale.

Tube length $L\ (cm)$	Tube diameter $d\ (cm)$	Wall thickness $w\ (mm)$	Pressure head $h_0\ (cm)$
90.4	9.78	0.16	10

Table 2: Dimensions of the oscillating water column and PTO at model scale.

OWC diameter $2r\ (cm)$	OWC length $l\ (cm)$	Chamber height $h_1\ (cm)$	Orifices diameter $d_0\ (mm)$
7.22	15.2	57.5	5.4 – 17.2

3. Wave generation and data-acquisition

The wave generator is a bottom-hinged paddle which is driven by a DC electrical motor with controllable speed. Its eccentric disk had to be modified in order to generate very small amplitude waves with a minimum wave height of 1 mm, as well as finite amplitude waves up to 80mm wave height. The wave frequency bandwidth imposed is $0.54 - 1.82$Hz. The wave flume and physical model are equipped with four water level sensors that allow for measurements of wave height upstream and downstream of the model when needed, as well as of OWC free-surface displacement z(t). The measurement uncertainty of these probes is ±0.5mm. Two of them are positioned between the wave generator and the physical model and one is positioned behind, towards the beach. The fourth probe is placed along the axis of the vertical duct. All probes are controlled by a four-channel HR wave-probe monitoring system from Wallingford. The output signals from the 4 water level probes have been logged at 200 Hz for 15s , by a KUSB-3100 S data acquisition card from Keithley and stored on disk. The wave field upstream of the model is equally surveyed with the help of a digital RT oscilloscope TDS220, from Tektronix. A PC 64-bit Pentium Dual-Core CPU E5700 at 3GHz with 4 GB RAM deals with the data processing. Testpoint V7 is used for data acquisition, instrument control and analysis. In order to determine the incident wave field a reflection analysis algorithm is used to separate the incident and reflected waves [10]. The results presented herein are derived from the fundamental components of the measured wave height and OWC surface elevation records, extracted by Fourier analysis.

In real sea conditions the prototype device is expected to cope with sea waves of roughly 5 to 12 s wave period and up to 5m wave height. This scales down at 1:70 to waves of T = 0.6 − 1.4s and H up to 7.1 cm wave height. A total of six series of regular waves of nondimensional wavenumber kh = 0.67 − 4.38 have been generated in the flume. They cover a range of wave periods T = 0.56 − 1.85s and wavelengths = 0.47 − 3.11m, in water of finite depth h = 0.33m. Table 3 details the ranges of wave period T, wavenumber K, wave height H and wave celerity Pi, together with incident wave power Pi which is taken to be the average energy-flux of the incident waves per unit wave crest. In water of finite depth h:

$$P_i = \frac{\rho_1 g H^2 \lambda}{8T} \frac{1}{2} \left(1 + \frac{2kh}{sinh(2kh)}\right) \tag{1}$$

In this expression H is the wave height, the wavelength, T the wave period, p1 the mass density of water and k is the fundamental wave number. Wave series 1 and 2 correspond to small amplitude waves having kH < 0.2, while wave series 3 to 6 have finite amplitudes for periods roughly bellow T = 1 s.

Table 3: Incident wave-fields generated at model scale.

Wave series	T (s)	k (m^{-1})	H (cm)	c (m/s)	P_i (W/m)
1	0.56 – 1.85	2.02 – 12.76	0.3 – 1.4	0.878 – 1.668	0.020 – 0.099
2	0.56 – 1.85	2.02 – 12.72	0.5 – 2.9	0.880 – 1.665	0.051 – 0.447
3	0.57 – 1.76	2.14 – 12.55	1.4 – 4.5	0.869 – 1.672	0.297 – 1.078
4	0.56 – 1.74	2.17 – 12.84	3.2 – 6.1	0.863 – 1.672	1.169 – 3.002
5	0.55 – 1.85	2.02 – 13.25	3.7 – 7.1	0.862 – 1.671	1.272 – 3.919
6	0.55 – 1.73	2.19-13.27	4.6 – 6.6	0.866 – 1.667	1.817 – 5.284

4. Tuning the model to the incident waves

The system's working principle makes use of the wave-excited pressure bulges in a distensible tube, which thereafter activate OWC oscillations of amplitude n in a forward bent duct. In the present case these periodic water oscillations are utilized to extract useful power by means of a pneumatic power take-off of adjustable impedance. The intensity of the bulges grows along the length of the tube towards the inlet of the duct and is dependent on the incident wave frequency. It has been demonstrated in [4] that resonant conditions may be achieved in the tube if the celerity of the incident waves equals the speed of the pressure bulges. In practice the tuning of a distensible tube can be met by choosing the appropriate material, tube diameter and wall thickness.

As given in [11] the bulge wave speed U inside the rubber tube is $U = 1/\sqrt{\rho_1 D}$, in the absence of hysteresis, where D is the distensibility of the tube. For a tube with circular cross-section of diameter d and wall-thickness w, $D = d/(wE)$; E is the Young's modulus of the tube material, which for latex at 100% strain is $E = 0.91\ MPa$. Hence, the free bulge-wave speed inside the tube is given by $U = \sqrt{wE/\rho_1 d}$. Now, as already mentioned the tuning of the system occurs when the speed of the longitudinal waves in the tube matches the celerity of the surface waves c outside. For $U = c$ the thickness of the tube must then be $w = \rho_1 c^2 d/E$, where $c = (gT/2\pi)\ tanh(kh)$ is the phase velocity of the incident waves in a water depth h. For the present physical model, whose tube dimensions are given in table 1, the expected free bulge-wave speed in the tube is $U = 1.22\ m\ /\ s$ and the corresponding bulge-wave tuning period to be met by the incident surface waves is $T_1 = 0.81\ s$.
Considering next harmonic oscillations of the water column inside the vertical duct, in the absence of the tube, a first approximation the OWC undamped natural period is $T_0 = 2\pi\sqrt{l/g}$. Here l is the length of the water column, measured from the inlet of the PVC elbow till the OWC free-surface. l being currently $15.2\ cm$, $T_0 = 0.78\ s$. In Fig. 2 both the OWC natural period T_0 and the tube's tuning T_1 are represented, for the range of incident wave periods tested. As can be seen, the tube's tuning period is in this case quite close to the OWC natural period. In full-scale, an OWC-connected distensible tube with $d = 6.85\ m$ and $l = 10.64\ m$ will become resonant with incident waves having a period $T = 6.5 - 6.8\ s$. This corresponds to incident wavelengths between $65\ m$ and $70\ m$.

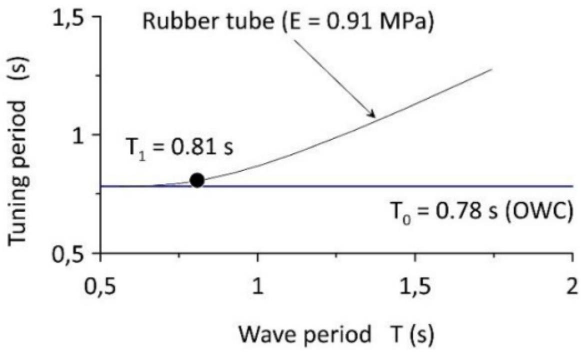

Figure 2: OWC natural period T_0 and tube tuning period T_1 as a function of incident wave period T, for $h = 0.33\ m$.

5. Amplification factor

Aiming to get a response that is as much as possible independent from the influence of the wave flume, an amplification factor ζ has been determined as a function of wave period. This factor is defined as the ratio between the mean water column oscillation height 2η and the incident wave height H. It is represented in Fig. 3 for the system operating nearshore over a sloped bottom. The water-column oscillation height reaches a maximum of 5.6 times the incident wave height near where the incident wavelength is twice the tube's length ($\lambda = 2L$), under the small amplitude waves of series 1. In essence, in order to achieve an amplification factor between 3 and 6 times the incident wave height, a prototype of this device would require a 63 m long tube operating under waves of period $T = 10\,s$, which corresponds to an incident wavelength of about $126\,m$. Note that the typical values of maximum amplification factor for OWCs without a distensible tube lie between 2 to 4.

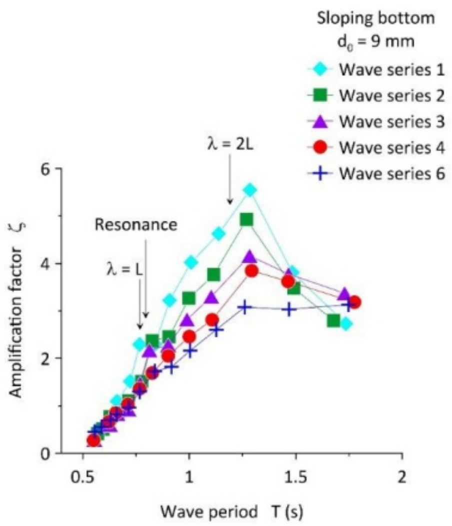

Figure 3: Amplification factor ζ as a function of the incident wave period T, for the nearshore system over a sloping bottom.

6. Pneumatic PTO characteristic

In the present experiment the pneumatic PTO consists of an air chamber which is connected to the atmosphere through a sharp-edged orifice of diameter d_0, bored in a $5\,mm$ thick plate. The air chamber is cylindrical, with cross-sectional area $A = 40.94\,cm^2$ and height $h_1 = 57.5\,cm$, measured from the still water level inside the vertical duct till the orifice. Let V be the volume of air entrapped in the control volume of the pneumatic chamber represented in Fig. 4, which is $V = 2.354\,dm^3$ in this case, and ρ its mass-density at ambient temperature. The corresponding mass of air in the chamber is $m = \rho V$, with $\rho = \rho(p)$ at constant temperature. The decrement in volume caused by a small rise of the water free surface *sl* is $dV = -Adz$ and, neglecting compressibility, the corresponding rate of change of air mass displaced by the water piston will be:

$$\frac{dm}{dt} = -A\rho\frac{dz}{dt} \tag{2}$$

By continuity, the rate of change of mass in the control volume $dm\,/\,dt$ equals the symmetric of the mass flow rate through the orifice. Taking A_0 as the cross-sectional area of the *Vena-contracta*, where the velocity is $v(t)$ toward the atmosphere, we extract from eq. (2):

$$v(t) = \frac{A}{A_0}\frac{dz}{dt} \tag{3}$$

For incompressible conditions the volume-flow rate of air across the orifice is then simply $Q = A(dz/dt)$, where dz/dt is the measured water free-surface velocity in the vertical duct.

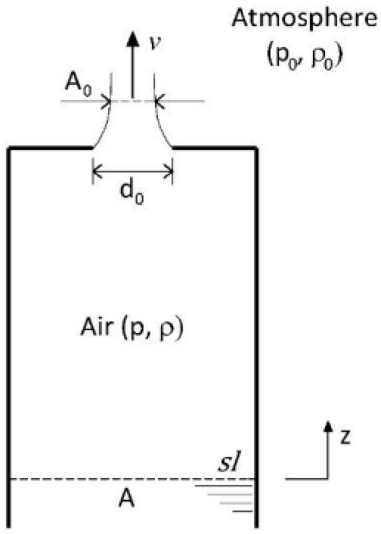

Figure 4: Control Volume of the pneumatic chamber.

If we now apply Bernoulli's law for steady incompressible flow along a streamline exiting from the Control Volume of the pneumatic chamber, the pressure drop Δp across the orifice is:

$$\Delta p = k_0 \frac{1}{2}\rho v^2 \tag{4}$$

where $\Delta p = |p - p_0|$ is the pressure difference between the chamber and the atmosphere, k_0 is the local loss-coefficient and v is the mean flow velocity at the *Vena-contracta*. Assuming a small orifice $(A_0/A \ll 1)$, the velocity of the flow in the jet is given by the following expression:

$$v = \pm \frac{1}{\sqrt{1+k_0}}\sqrt{\frac{2\,\Delta p}{\rho}} \tag{5}$$

Here the factor $1/\sqrt{1+k_0}$ is the so-called velocity coefficient, which considers the local resistance to the flow. Recall that p is the pressure in the pneumatic chamber, p_0 is the ambient pressure outside and that uniform flow across the *Vena-contracta* has been assumed.

Based on the air velocity given by eq. 5, the volume flow Q through an orifice of diameter d_0 takes the form:

$$Q = C\ \frac{\pi d_0^2}{4} \sqrt{\frac{2\ \Delta p}{\rho}} \tag{6}$$

In this equation $C = \varepsilon/\sqrt{1 + k_0}$ is a discharge coefficient, where ε is the ratio between the section areas of the *Vena-contracta* and the orifice. The pressure to volume-flow characteristic of the present PTO can finally be derived from this last expression and written as follows:

$$\Delta p = KQ^2, \text{where } K = \frac{8\rho}{C^2\pi^2 d_0^4} \tag{7}$$

The constant K is known as the orifice characteristic. Given the assumptions stated above, a reasonable empirical value for the discharge coefficient of a small hole in a plate is $C = 0.6$, thus resulting in a value of $K = 2.53 d_0^{-4}$ for ambient air at 945 $mbar$ and 20 ℃.

In Fig. 5 a PTO characteristic curve has been derived from the fundamental component of displacement measurements $z(t)$, using eq. 7 with $C = 0.6$. It corresponds to the system shown in Fig. 1 with an orifice with diameter $d_0 = 9\ mm$ and all the wave series tested. For a mean volume-flow rate between 0 and 61 l/min the pressure in the pneumatic chamber rises to about 497 Pa, following a typical impulse turbine characteristic.

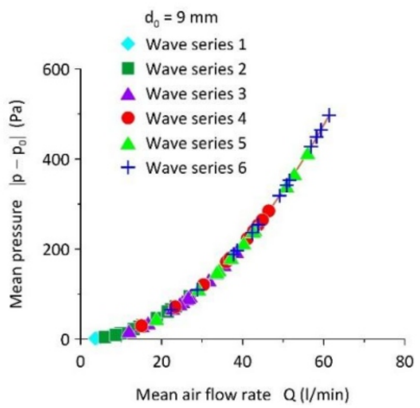

Figure 5: Pressure to volume-flow characteristic of the power take-off system.

7. Extracted power and capture-width

The instantaneous power extracted at the orifice is given in adiabatic conditions by the air flowrate across the orifice $Q(t)$ times the differential pressure $\Delta p(t)$. Hence, the mean power P extracted by the system at each stroke with period T is:

$$P = \frac{1}{T} \int_0^T |\Delta p(t)| \cdot |Q(t)|\ dt \tag{8}$$

Based on the values obtained for the mean extracted power P and the incident wave power per unit wave front P_i, a suitable measure of the system's efficiency is the well-known energy capture-width C_W. It may be defined in tube diameters as follows:

$$C_W = \frac{P}{P_i d} \tag{9}$$

Depicted in fig 6 is the capture-width C_W of the system operating nearshore, with a PTO orifice of diameter $d_0 = 9\ mm$, as a function of wave period T. Out of all the different orifice diameters tested in order to search for a near-optimal PTO impedance rate, the orifice with $d_0 = 9\ mm$ yielded the best energy capture efficiency. The capture-width C_W attains a maximum of 1.78 tube diameters at resonance under waves of series 3. Except for the waves of series 1, whose maximum C_W occurs where $\lambda = 2L$, the peak efficiency happens at resonance near where $\lambda = L$. Here the tube oscillates with a third mode of bending – see Fig. 7. Actually, the small amplitude waves of series 1 are unable to excite this bending mode and thus the capture-width remains under 1 tube diameter at $T = 0.8\ s$. As expected, for waves with significant wave height the effects of the sloping bottom are more important for larger wavelengths, where the waves are influenced by the water depth, contributing to raise the capture-width C_W when $\lambda = 2L$. It is found that the coupling between the bulges in the tube and its bending modes is important, especially at the period where the incident wavelength is equal to the tube length ($T = 0.77\ s$), quite close in this case to T_0 and T_1. This is indeed a determining factor of the system's maximum efficiency. Equally important is the period where $\lambda = 2L$, as confirmed by the amplification factor ζ (Fig. 3).

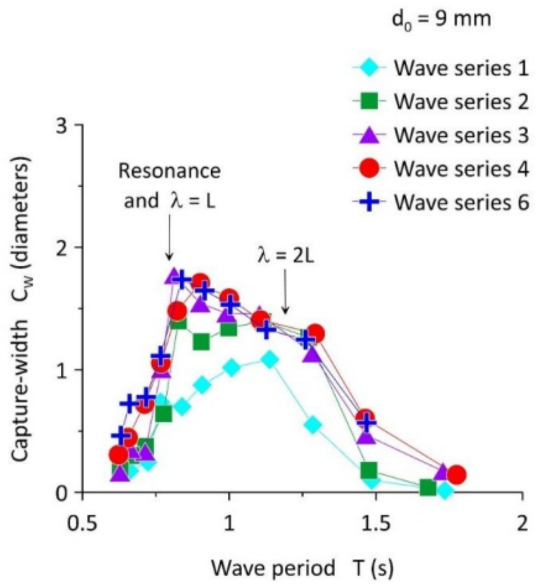

Figure 6: Capture-width C_W as a function of incident wave period T, for the model over a sloping bottom with a PTO orifice of diameter $d_0 = 9\ mm$.

Figure 7: Tube's fully developed third-mode of bending.

8. Onshore system in a sea-wall

Fig. 8 represents the distensible tube system fitted into a reflecting barrier. This model enables to test the system in the onshore configuration in water of variable or constant depth and compare the results with the nearshore configuration of Fig. 1.

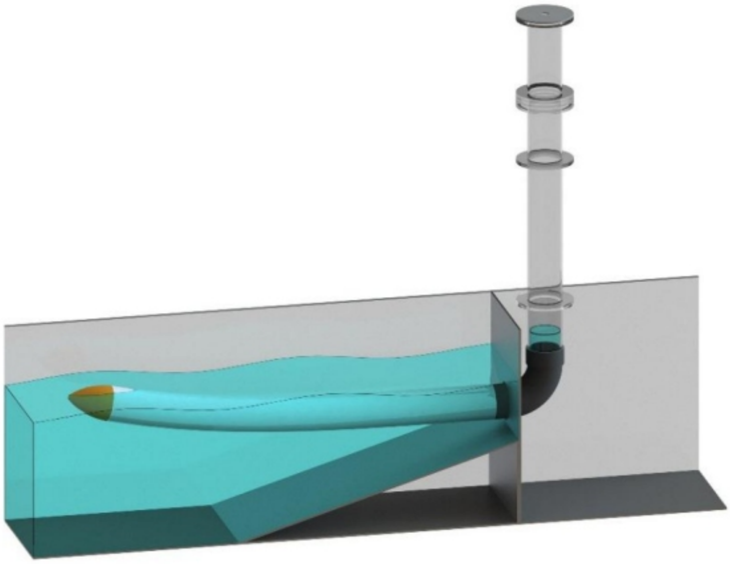

Figure 8: Distensible-tube wave attenuator fitted into a reflecting wall over a 30.1% slope removable bottom.

A comprehensive comparison is made between the nearshore and onshore situations previously studied, whose energy capture efficiency is consolidated in fig. 9 for wave series 1, 2, 4 and 6. In terms of capture-width neither the water-depth variation nor the inclusion of a reflecting barrier bring foreseeable efficiency improvements bellow $T \approx 0.77\ s$. Above this period the barrier at constant water-depth leads to an increase in maximum capture-width of at most 28% relative to the nearshore system on a sloped bottom, for the highly energetic waves of series 4 and 6. The system fitted on a sea-wall over a sloping bottom is capable of attaining an even higher maximum capture-width, reaching 2.26 tube diameters at $T = 1\ s$ for the waves of series 6. The influence of a sloping bottom is twofold: on one hand it amplifies the height of the incident waves as they travel along the tube towards the barrier; on the other hand it gives rise to a second mode of bending of the tube when $\lambda = 2L$, which increases the bandwidth of high capture-width. The bending modes at $\lambda = L$ and $\lambda = 2L$ are relevant in determining not only the peak efficiency, but also the bandwidth where $C_W > 1$. It is worth noting that the barrier over constant depth is unable to excite the bending mode at $\lambda = 2L$ for the small amplitude waves of series 1 and 2. All these considerations become pivotal when designing a nearshore or onshore application.

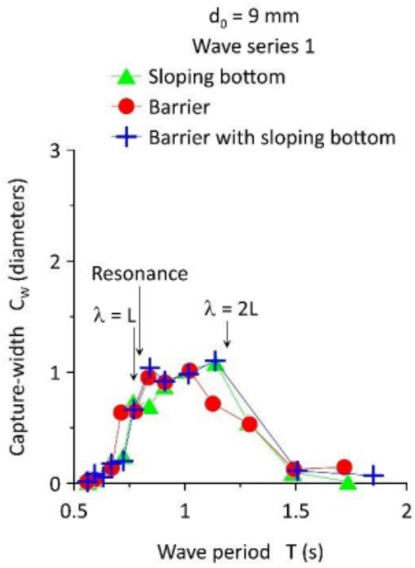

(a)

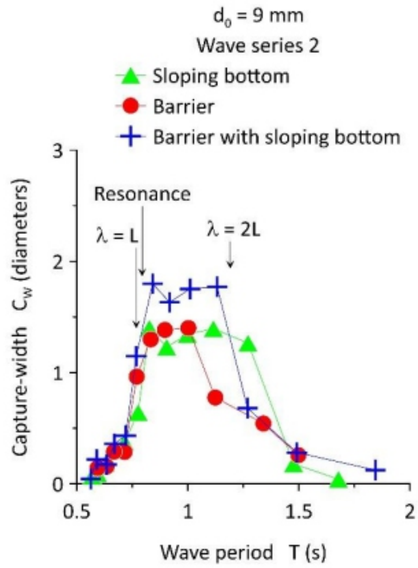

(b)

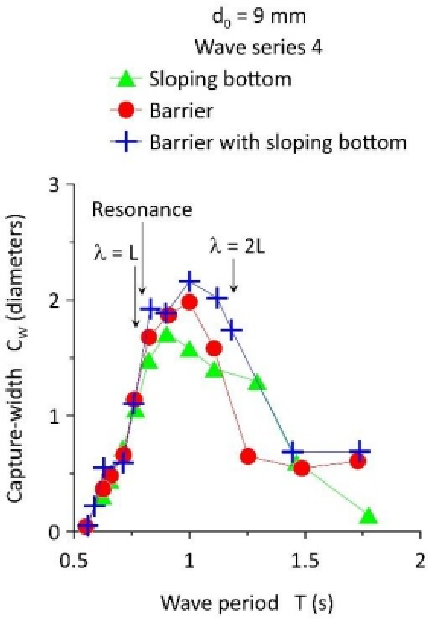

(c)

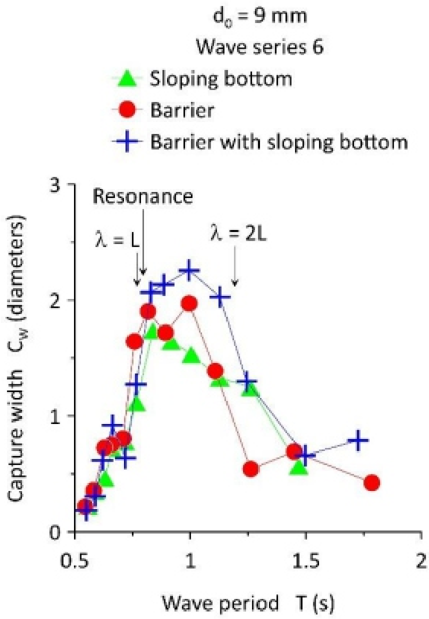

(d)

Figure 9: Capture-width C_W versus wave period T for the nearshore and onshore configurations studied under wave series 1 (a), wave series 2 (b), wave series 4 (c) and wave series 6 (d).

9. Hydrodynamic and overall efficiencies

An energy balance which comprehends a far-field analysis of the reflected and transmitted waves, together with the extracted power at the PTO is now accomplished. The wave measurements have been performed sufficiently far from the model so that evanescent modes had decayed. Part of the incident wave energy is transferred to the system at its primary interface, with the remaining fraction being reflected and transmitted by the tube oscillations or lost due to viscosity. A reflection analysis of the waves upstream yields the total reflection coefficient R and the transmission coefficient T_r is monitored by the wave probe downstream of the model. The system's hydrodynamic efficiency is then $1 - R^2 - T_r^2$. In order to complement the performance assessment of the system, an overall efficiency is also defined as the ratio of the extracted energy PT to the incident wave energy over the width of the flume. Fig. 10 gathers these two efficiencies as a function of the incident wave period for the onshore system in a sea wall over a sloping bottom of Fig 8. The hydrodynamic efficiency is maximum at resonance ($T = 0.81\ s$), almost reaching 1, and falls dramatically as the wave period increases. It is known that the energy losses are larger for waves of small periods, decreasing monotonously as the wave period increases. As a consequence, the overall efficiency attains a maximum of 0.48 between $T = 0.81\ s$ and $T = 1\ s$. In practice the system extracts at most 48% of the total wave power available in a wave front equal to the flume width. For wave periods under the system's resonance the hydrodynamic efficiency is very high and the overall efficiency is poor. This difference reflects a surplus of energy which is not converted into useful power, in part due to wave breaking over the nose and on top of the tube (see Fig. 11) as well due to other energy dissipation mechanisms.

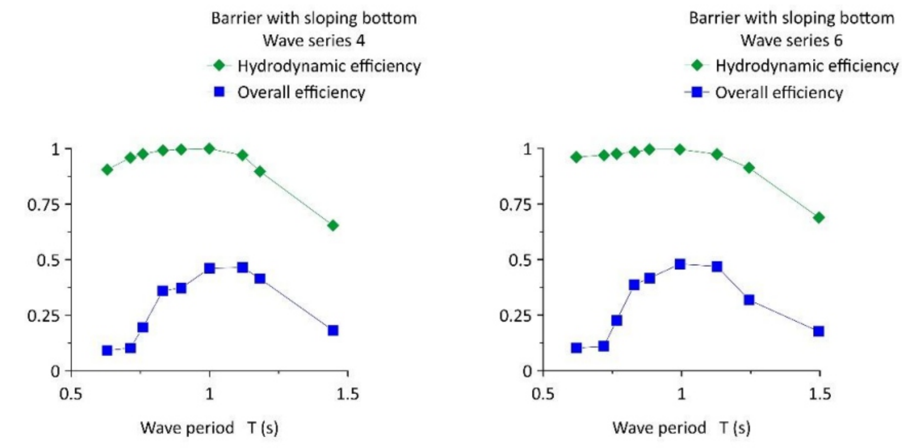

(a) (b)

Figure 10: Hydrodynamic and overall efficiencies of the system fitted on a sea-wall over a sloping bottom, as a function of wave period T, obtained with an orifice of diameter $d_0 = 9\ mm$ under wave series 4 (a) and wave series 6 (b).

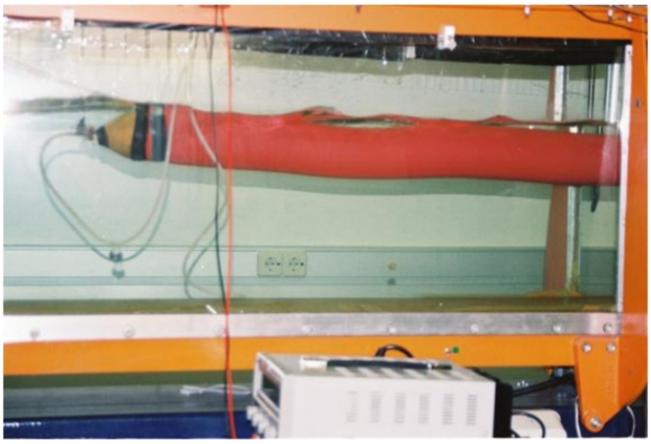

Figure 11: Interference of the incident waves with the tube and flume side-walls.

10. Summary and conclusions

The present research focuses on the performance assessment of a simple and low-cost device which can be deployed at the nearshore or onshore, incorporating well-tried rubber and turbine technologies. To that end a 1:70 scale model of an OWC-connected water filled distensible tube has been tested in a wave flume, freely floating head to regular waves. Air compressibility has been neglected, an assumption that is to some extent valid for small-scale laboratory work. A total of sixty waves per PTO impedance have been generated in the wave flume that correspond to the envisaged nearshore wave conditions. In each wave series 23% were deep water waves and 77% were intermediate waves. In full-scale they translate to waves with periods from 4.6 s to 15.5 s and up to 5 m wave height.

A prototype of the device is foreseen to utilize a rubber tube roughly 63 m long with about 7 m in diameter. The bulge-wave tuning period scales to 6.8 s, which corresponds to waves having a wavelength of about 70 m propagating in a water depth of 23 m. Coincidently, the natural frequency of the oscillating water column is at 6.5 s. Moreover, when the incident waves have a wavelength twice the length of the tube, i.e. about 126 m, a resonant bending mode is also apparent which proves to be beneficial for wave energy extraction. The maximum energy capture-width attained is 2.26 tube diameters for the most energetic waves and it occurs close to the tube tuning, for the onshore configuration. For the nearshore configuration it does not exceed 2. Under these conditions the tube oscillates with an extra surging motion, apart from significant bending and bulging. When operating near the tube tuning under waves of 3.5 m wave height, the onshore system is then able to capture the energy of a 15.5 m long wave front in average. When under waves of smaller wave height, of the order of 0.5 m, the tube is instead sensitive to wavelengths of about 126 m, which is twice the length of the tube in full-scale. In general, the system is efficient ($C_W > 1$) for a large range of sea waves with periods roughly between 6 s and 11 s. The effect of a sloping bottom is beneficial and results in tube bending modes which also resonate when $\lambda = 2L$. A relevant aspect is that the onshore system fitted in a sea wall, over a sloping bottom, responds efficiently not only to waves with wavelength of the order of two times the tube length but also in resonant conditions.

Acknowledgments

The present research was conducted in the Laboratory of Fluid Mechanics and Turbomachinery at Universidade da Beira Interior, in Portugal. The work was partially funded by The Portuguese Foundation for Science and Technology and The European Union. The authors are grateful to the Emeritus Professor John Chaplin (University of Southampton) for sharing his expertise on the subject. The skills and goodwill of Mr. Morgado demonstrated during the manufacture of the physical model are also acknowledged.

References

[1] World Energy Council, 2016, "World Energy Resources – Marine Energy",London. [Online] Available:http://large.stanford.edu/courses/2018/ph240/rogers2/docs/wec-2016.pdf

[2] Foley, M. and Whittaker, T. J. R., 2009, "Analysis of the Nearshore Wave Energy Resource", Renew. Energy, 34, pp. 1709-1715. DOI:10.1016/j.renene.2009.01.003

[3] Farley, F. J. M. and Rainey, R. C. T., 2006, "Distensible Tube Wave Energy Converter", British patent N. GB 2434840, UK Intellectual Property Office.

[4] Chaplin, J. R., Farley, F. J. M. and Rainey, R. C. T., 2007, "Power Conversion in the Anaconda WEC", in Proc. of the International Workshop on Water Waves and Floating Bodies, 4 pp., Plitvice.

[5] Chaplin, J. R., Farley, F. J. M., Prentice, M. E., Rainey, R. C. T., Rimmer, S. J. and Roach, A. T., 2007, "Development of the Anaconda All-Rubber WEC", in Proc. of the 7 th European Wave and Tidal Conference, Ed. A. F. Falcão et al., 13 pp., Porto.

[6] Chaplin, J. R., Farley, F. J. M., Hearn, G. E., Heller, V. and Mendes, A., 2010, "Hydrodynamic Performance of the Anaconda Wavepower Device", in Proc. of the HYDRALAB III Closing Event, Hannover.

[7] Chaplin, J. R., Heller, V., Farley, F. J. M., Hearn, G. E. and Rainey, R. C. T., 2012, "Laboratory Testing the Anaconda", Philos. Trans. Royal Soc. A, 370, pp. 403-424. DOI:10.1098/rsta.2011.0256

[8] Mendes, A. C., Paredes, L. M. A., Gil, F. A. S. and Chaplin, J. R., 2014, "SmallScale Model Tests of a Rubber-Tube Wave Energy Converter with Pneumatic Power Take-Off", in Proc. of the ASME 33rd International Conference on Ocean, Offshore and Arctic Engineering, San Francisco. DOI:10.1115/OMAE2014- 23452

[9] Evans, D. V. and Porter, R., 1997, "Efficient Calculation of Hydrodynamic Properties of OWC-Type Devices", J. Offshore Mech. Arct. Eng., 119(4), pp.210-218. DOI:10.1115/1.2829098

[10] den Boer, K., 1981, "Estimation of Incident and Reflected Wave Characteristics of Perpendicular Wave Action", Research report S 434, Vol. I, Delft Hydraulics Laboratory, The Netherlands.

[11] Lighthill, J., 1978, "Waves in Fluids", Cambridge University Press, Cambridge.

Improvement of the Airflow Alignment in an Automotive Brake Disc Through a Naca 2411-Il Profile Using Computational Fluid Dynamics (Cfd).

Cesar Iram Aldaz, Francisco Carrillo, Raúl Ñeco, Mayra Ocampo
Instituto de ingeniería y tecnología, Universidad Autónoma de Ciudad Juárez, Avenida del charro 450 norte, Ciudad Juárez Chihuahua, México C.P. 32315

ABSTRACT

In the present study, we investigate the improvement of airflow alignment in brake discs through the application of NACA profiles. Efficient ventilation is crucial to avoid problems such as overheating and brake fading. Using Computational Fluid Dynamics (CFD) simulation with ANSYS Fluent, we compare the traditional geometry of a brake disc with a proposal that incorporates NACA profiles. Our results demonstrate a clear advantage in terms of airflow alignment with the proposed geometry, suggesting significant potential for improving brake performance. This study sheds light on a promising innovation in the automotive industry and its implications for road safety and vehicle efficiency. The results obtained in this study provide insight into the fluid dynamics in the brake disc, including differences in velocity distribution and a more uniform pressure distribution. The proposed geometry has the potential to offer improvements compared to the original geometry.

Keywords: Brake disc, CFD, NACA profile, ventilated disc, fluid flow.

INTRODUCTION

One of the fundamental systems in an automotive vehicle is its braking system, as its primary responsibility lies in ensuring the safety of the occupants, regardless of prevailing environmental conditions. In this study, a brake disc from a 2008 Nissan Versa Hatchback was used, characterized by its straight ventilation design incorporating 36 thermal dissipation fins. However, to optimize its performance, these fins were replaced with 25 NACA-type profiles. The vehicle in question is equipped with tires of dimensions 185/65/R15 and has a mass of 1251 kg. The disc's construction material is gray cast iron, with a machined surface and a fastening system consisting of four bolts.

A drum brake system is used in the rear section. It is worth noting that both discs were replicated in a virtual environment using SolidWorks mechanical design software.Within the framework of the analysis conducted by [1], regarding the thermodynamic study of an automotive brake disc with NACA 66-209 type ventilation pillars, the effectiveness of the braking system was confirmed in various climatic conditions, considering the employed NACA profile configuration. Conversely, [2] conducted a meticulous analysis of the heat exchange flow between the cooling channels of three brake discs. Under operational conditions of 80 km/h, optimal behavior in terms of temperature, velocity, and heat flow in the ventilation ducts was observed. Relevant research, such as that conducted by [3], involved a dynamic analysis of three ventilated disc brakes through numerical simulations using SolidWorks Simulation software. This study demonstrated that the third brake disc design proposal exhibited superior performance under various working conditions, including speed and displacement during the braking process in the cooling channels. Additionally, [4] explored the velocity field measurement in the suction and discharge of an automotive brake disc with drop-shaped ventilation pillars, using the particle image velocimetry technique. He proposed NACA 4418 and 66-219 profile geometries in this configuration, obtaining optimal results. In another line of research, [5] conducted a thermodynamic analysis of three ventilated disc brakes using finite element analysis (FEM) at a constant vehicle speed of 80 km/h. In this investigation, both heat dissipation velocity and heat extraction temperature were evaluated, taking into account the material properties used in the discs. On the other hand, [6] conducted an exhaustive review of Computational Fluid Dynamics (CFD) applications in the automotive industry and their influence on the design of automotive components. It was concluded that incorporating CFD in the initial design stages is imperative to minimize subsequent modifications and corrections. [7] anticipated the cooling factors of an automotive brake disc and analyzed their impact on the results of thermal numerical simulations. The obtained results revealed a substantial effect on temperature, emphasizing the importance of incorporating accurate heat transfer coefficients in simulations to obtain reliable results.

METHODOLOGY

En Figure 1, the specific brake disc chosen for this research is presented. To provide a more detailed understanding of this brake disc, Figure 2 displays its precise dimensions, carefully annotated in millimeters. These dimensions include the outer diameter, inner diameter, disc thickness, as well as the strategic placement of slots and ventilation holes. Each of these measurements is of critical importance in assessing fluid dynamics.

Figure 1. The disc belongs to a 2008 Nissan Versa hatchback. Source: Authors.

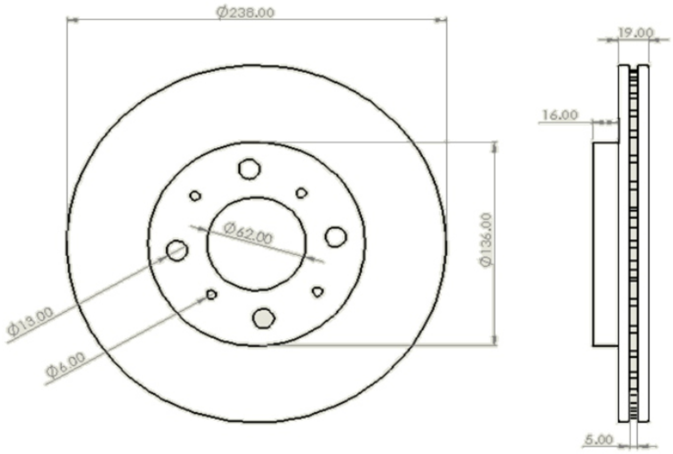

Figure 2. Brake disc dimensions, annotated in mm. Source: Authors.

The purpose of this study is to modify the original design of the brake disc, which incorporates cooling channels characterized by rectangular profiles. The central focus of the research is the evaluation of fluid dynamics in the system after replacing these profiles with an aerodynamic design based on the NACA profile. The geometric description of this new profile is presented below.

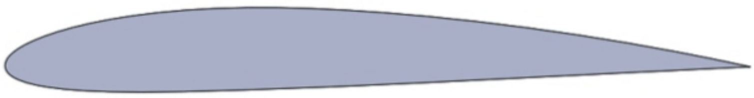

Figure 3. NACA 2411-il Profile. Source: Authors.

Table 1. Profile Characteristics.

NACA 2411 aerodynamic profile
Maximum thickness from 11% to 29.5% of the chord.
Maximum camber from 2.5% to 39.6% of the chord.

Source: http://airfoiltools.com/airfoil/details?airfoil=naca2411-il.

SolidWorks mechanical design software was used to model both the original brake disc and the alternative proposal. The detailed representation of both models is illustrated in Figure 4.

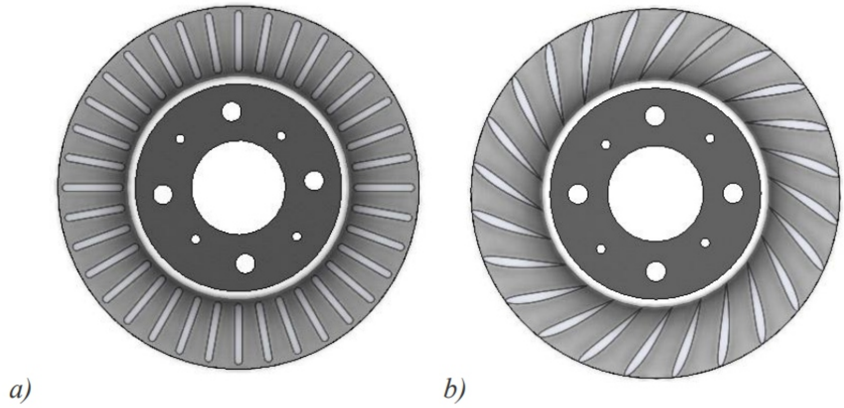

Figure 4. Brake disc a) original model b) proposal. (Source: Authors).

For the simulation, ANSYS Fluent software was chosen, and the decision was made to use a mosaic mesh. This choice is based on its high flexibility, allowing it to adapt effectively to highly complex geometries. Additionally, this mesh provides the ability to generate a highly accurate discretization, capturing the local details present in the geometry under analysis meticulously. It is worth noting that, compared to other meshing approaches, the mosaic type requires a lower number of elements, resulting in a significant reduction in computational load.

In summary, the selection of a mosaic mesh is justified by its versatility, ability to provide accurate discretization, and efficiency in terms of computational resources. Figure 5 shows the visual representation of the mesh used in this study, offering an illustrative detail of its structure.

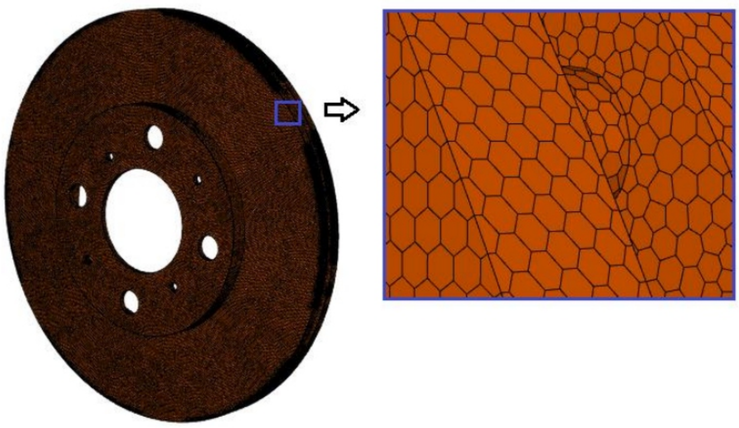

Figure 5. Meshing of the brake disc. (Source: Authors).

In our analysis, we conducted a mesh convergence study to validate the choice of the mesh used. This process is crucial in numerical simulation as it ensures that the selected mesh is most suitable for accurately representing the behavior of the brake disc. The convergence of results, confirmed as we refined the mesh, conclusively supports that we have chosen the most suitable mesh to achieve highly accurate and reliable results in our engineering analysis of the brake disc. Figure 6 illustrates the computational domain used in this study. In the context of simulating the brake disc, a wall boundary condition has been implemented to represent the disc's surface. Additionally, air inlet and outlet conditions have been incorporated to model and analyze the flow through the system.

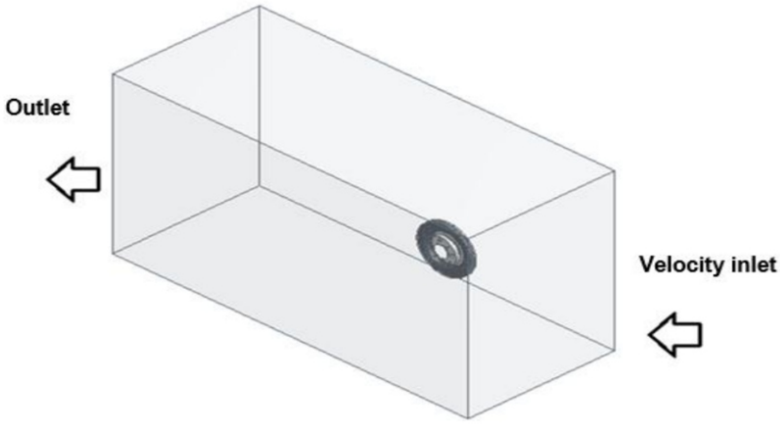

Figure 6. Computational domain. (Source: Authors).

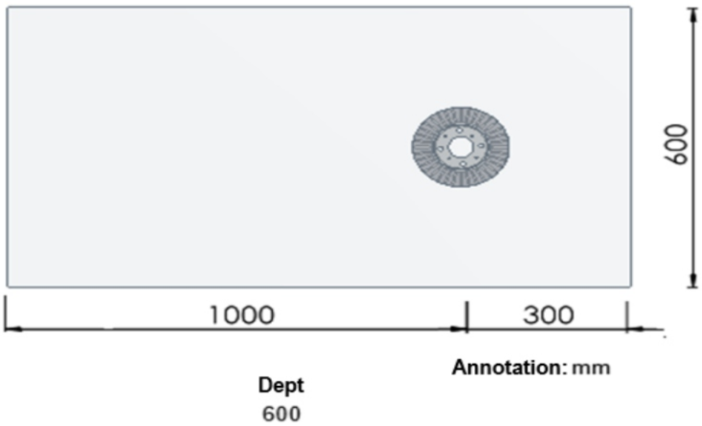

Figure 7. Domain dimensions. (Source: Authors).

Figure 7 depicts the dimensions used for the study. Three-dimensional (3D) simulations were chosen for their ability to capture critical three-dimensional phenomena and provide an accurate representation of the interaction between the brake disc geometry and the airflow. Since brake discs are 3D objects with non-uniform temperature and airflow distributions across their thickness and surface, 3D simulations allow for a precise assessment of heat transfer and aerodynamic resistance. In automotive and aerospace applications, where safety and performance are paramount, these simulations offer results closer to reality, supporting informed decision-making to enhance efficiency and safety in vehicles.

The choice of the k-epsilon turbulence model for this study is based on an extensive review of scientific literature, consistently highlighting its effectiveness in predicting turbulent flows in various contexts.

Numerous authors have reported that the k-epsilon model provides more accurate and representative results compared to other turbulence models in situations similar to those addressed in this study. The inlet velocity conditions in this study have been determined based on typical driving speeds in different environments. To represent driving in urban settings, an average speed of 60 km/h has been considered. Additionally, to simulate driving on highways, two additional scenarios have been evaluated, namely speeds of 90 km/h and 120 km/h. These speed selections are based on common driving patterns and reflect usage conditions encountered on highways and in urban areas.

Considering that:

$$1\ \frac{\text{km}}{\text{hr}} = \frac{1000\text{m}}{3600\ \text{s}} = 0.27778\ \frac{\text{m}}{\text{s}} \qquad (1)$$

Based on equation 1, it is possible to determine the inlet velocity boundary condition for each of the proposed speeds. In the case of tire rolling, a 80% adherence to the road surface is assumed, allowing the slip to be determined as:

$$x = \frac{(v_i - v_p)}{v_p} * 100 \qquad (2)$$

Where:

$$v_i = \text{Vehicle velocity.}$$
$$v_p = \text{Peripheral velocity.}$$

Once the peripheral speed is obtained, the angular velocity of the brake disc will be determined, taking into account its radius.

$$\omega = \frac{v_p}{r} \qquad (3)$$

Where:

$$\omega = \text{Angular velocity.} \frac{\text{Rad}}{\text{Seg}}$$
$$v_p = \text{Linear velocity.} \frac{\text{m}}{\text{s}}$$
$$r = \text{Brake disc radius. m}$$

Ultimately, the rotation speed of the disc was established, expressed in revolutions per minute (RPM), using Equation 4:

$$\text{RPM} = \frac{\omega}{2\pi} \qquad (4)$$

Table 2. Speeds.

Velocity			
Vehicle velocity (Km/h)	60	90	120
Air velocity inlet (m/s)	16.66	25	33.33
"Peripheral velocity of the disc." (m/s)	9.25	13.88	18.51
Rotational velocity of the disc (ω rad/seg)	69.97	104.96	139.95
Disc rotation velocity (RPM)	667.61	1004.92	1337.23

Source: Authors.

Table 2 presents the results derived from equations 1, 2, 3, and 4. These data will be used to establish boundary conditions for both the inlet velocity and the rotational speed of the brake disc. In the context of this research, the parameters used as references are the air inlet velocity and the rotational speed of the disc, measured in revolutions per minute (RPM).

RESULTS

A cutting plane was chosen to intersect the computational domain and pass through the disc, allowing for the visualization of its internal region.

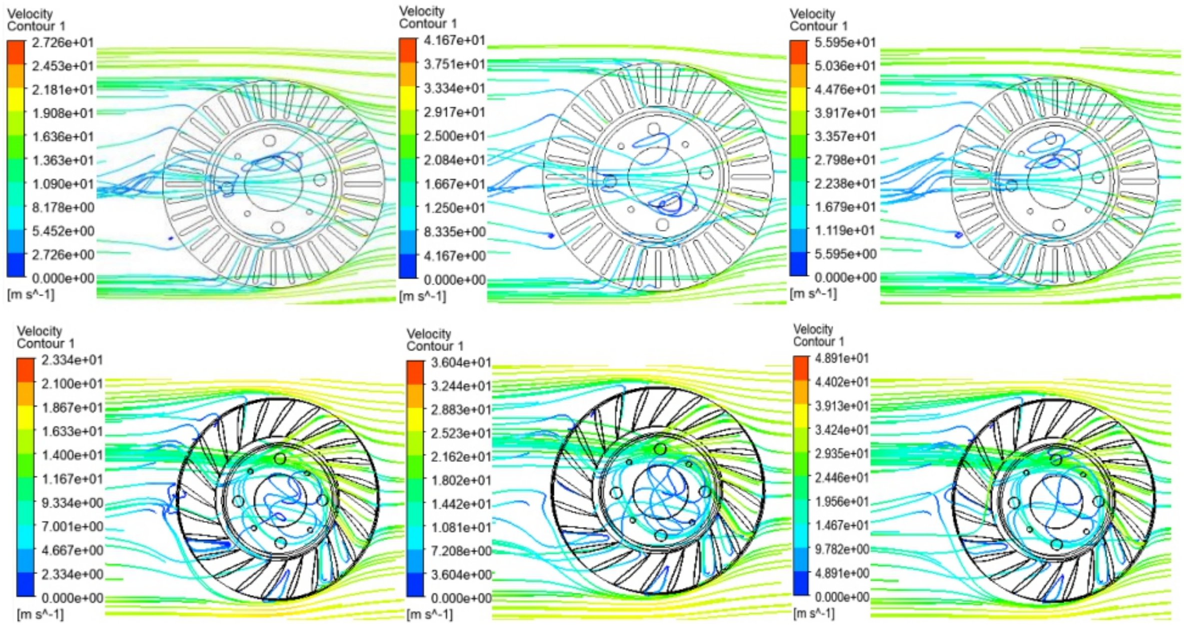

Figure 8. Streamlines of the original and modified disc, for speeds of 60, 90, and 120 km/h.

Source: Authors.

Figure 8 presents the streamlines generated for both the original and the proposed configurations. It can be observed that in the proposed design, the NACA profile facilitates the flow entering into the circulation channels, whereas in the original geometry, although it passes through the disc, it does not distribute adequately within that geometry.

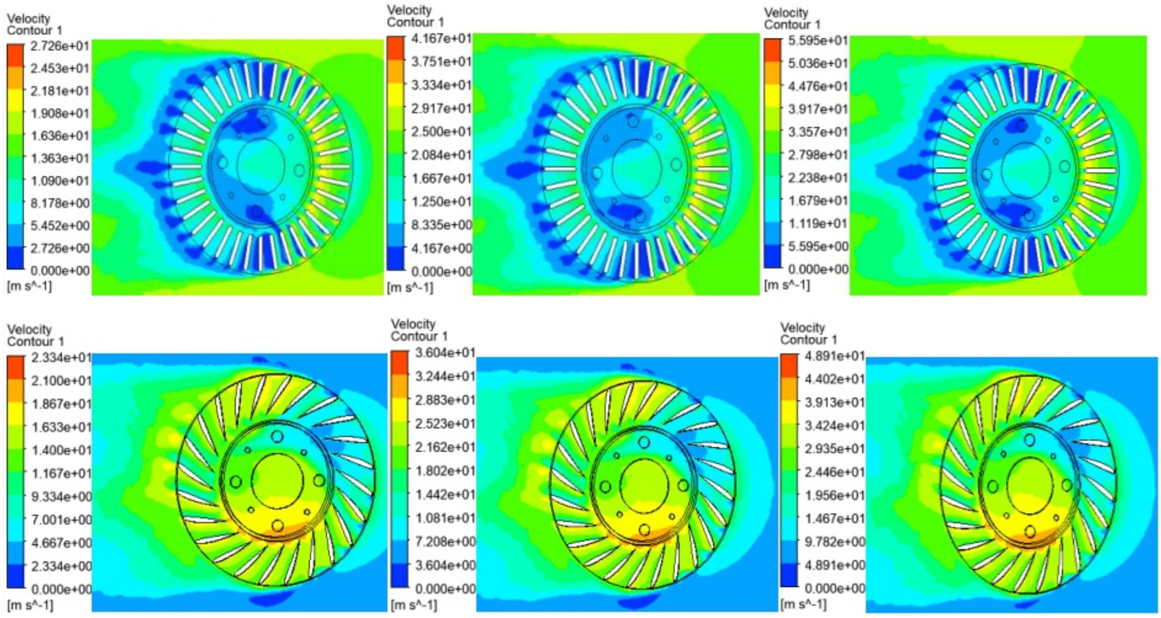

Figure 9. Velocity contours of the original and modified disc, for speeds of 60, 90, and 120 km/h. Source: Authors.

Figure 9 illustrates the behavior already evident in the streamlines. The velocity contours reveal a notable difference in speeds between the original geometry (downstream) and the proposed one. In the original geometry, a significantly lower speed is recorded compared to the proposal, where a more uniform velocity distribution is observed, albeit with a lower magnitude.

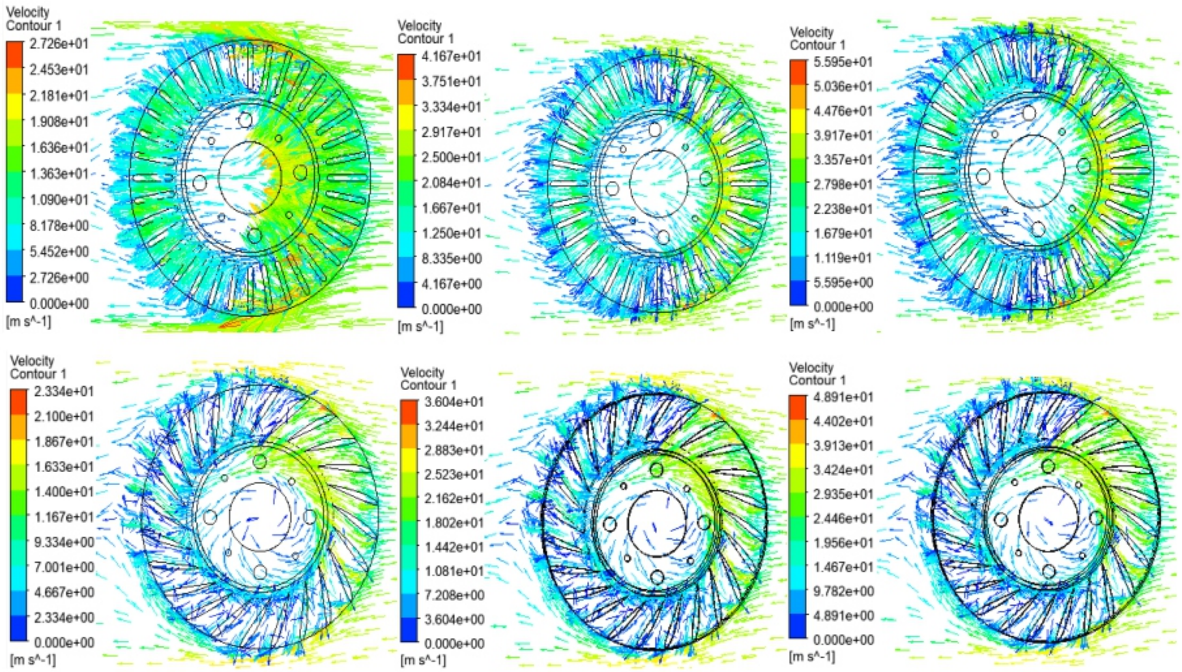

Figure 10. Velocity vectors of the original and modified disc, for speeds of 60, 90, and 120 km/h. Source: Authors.

The velocity vectors represented in Figure 10 show that, in the original geometry, these vectors follow a linear trajectory, while in the proposed design, they tend to adopt a rotational direction due to the influence of the NACA profile. This configuration facilitates the flow circulation along the cooling channel. It is important to note that, although a decrease in velocity magnitude is observed compared to the original geometry, this could be attributed to the circular nature of the path that the flow takes in the proposed design.

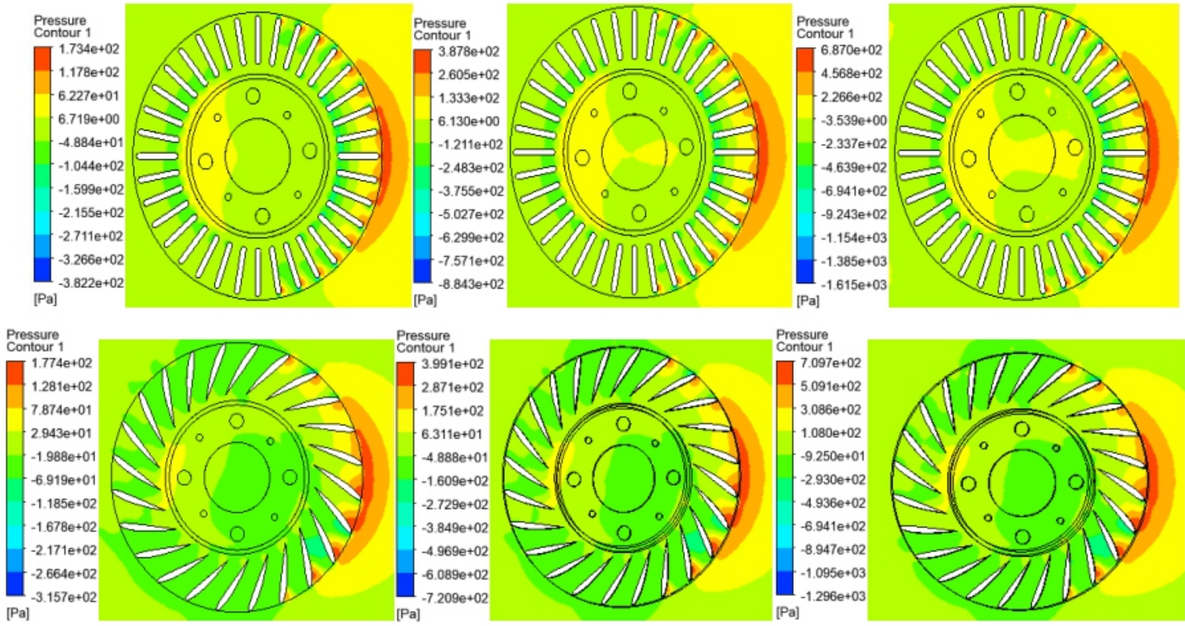

Figure 11. Pressure contours of the original and modified disc, for speeds of 60, 90, and 120 km/h.
Source: Authors.

The pressure contours depicted in Figure 11 reflect that the proposed configuration exhibits a pressure distribution in contrast to the original geometry. This observation indicates a potential improvement in heat dissipation capability. Additionally, a uniform pressure distribution may correlate with increased stability during the braking process, a decrease in the risk of unwanted vibrations or noise, and a reduction in fluid flow resistance.

CONCLUSIONS

Following the research and analysis process, the results obtained in this study provide insights into the fluid dynamics of the brake disc. Below, we will present the conclusions derived from the findings.

Differences in velocity distribution: Clear differences in velocity distribution are observed between the original and proposed geometries. The proposed geometry exhibits a more uniform velocity distribution across the area of interest compared to the original geometry, which shows less uniform velocity. This improvement in velocity uniformity in the proposed geometry suggests potential advantages in terms of flow and heat dissipation.

Effect of the NACA profile: In the proposed geometry, the influence of the NACA profile is reflected in the rotational direction of velocity vectors. This feature can be beneficial as it facilitates flow circulation along the cooling channel. The rotation of velocity vectors is an adaptation that implies a more efficient design for fluid circulation.

More uniform pressure distribution: Pressure contours in the proposed geometry show a more uniform distribution compared to the original geometry. This uniformity in pressure distribution is a positive indication as it may enhance heat dissipation capability and stability during braking. Additionally, it reduces the risk of unwanted vibrations and fluid flow resistance.

The results indicate that the proposed geometry has the potential to offer improvements in terms of velocity distribution, flow circulation, and pressure distribution compared to the original geometry. These improvements suggest a design that could be more efficient in heat dissipation and brake system performance, potentially positively impacting vehicle safety and efficiency.

REFERENCES

[1] García León, R. A., 2018, "Thermodynamic Analysis of an Automotive Brake Disc with NACA 66-209 Ventilation Pillars" INGE CUC. doi:10.17981/ingecuc.14.2.2018.01

[2] Pérez Rojas, E., 2016, "Analysis of the amount of heat flow between cooling channels in three vented brake discs " Ingenieria y Universidad. doi:10.11144/Javeriana.iyu21-1.aahf

[3] Hongbin, Y., 2015, "Analysis of the flow air on an automotive brake disc with profiles N-38 type" . doi:10.1016/j.applthermaleng.2015.08.042

[4] Garcia Leon, R. A., 2017, "Improvement of the mechanical properties of nodular gray cast iron with the application of heat treatments".doi:10.15446/ing.investig.v37n3.63381

[5] Jimenez Garcia, C. A.,2015,"MEASUREMENT OF THE VELOCITY FIELD IN THE SUCTION AND DISCHARGE OF AN AUTOMOTIVE BRAKE DISC WITH DROP-TYPE VENTILATION PILLARS, THROUGH PARTICLE IMAGE VELOCIMETRY (PIV)". Rivera, Jesús. Retrieved from [URL] https://cibimrevista1.wordpress.com/2015/11/13/mecanica-de-fluidos rivera-jesus/

[6] Garcia Leon, R. A.,2018, "Thermodynamic Analysis of an Automotive Brake Disc with NACA 66-209 Ventilation Pillars" INGE CUC. doi:10.17981/ingecuc.14.2.2018.01

[7] Chen Huang, Z.,2010," Laboratory observation of boundary layer flow under spilling breakers in surf zone using particle image velocimetry". doi:10.1016/j.coastaleng.2009.11.004

[8] Garcia Leon, R. A.,2016,"Thermal study in three vented brake discs, using the finite element analysis". doi:10.15446/dyna.v84n200.55663

[9] N, D. M. ,1996, "Review: CFD applications in the automotive industry".

doi:10.1115/1.2835492

[10] Pevec, M.,2012, "Prediction of the cooling factors of a vehicle brake disc and its influence on the results of a thermal numerical simulation" - International Journal of Automotive Technology. doi:10.1007/s12239-012-0071-y

[11] Karan, D.,2018, "Thermo-mechanical performance of automotive disc brakes".doi:10.1016/j.matpr.2017.11.287

[12] Rojas, V.,2020, " Analysis of the efficiency of a conventional ventilated brake disc compared to a hyper-ventilated disc through machining. Retrieved from: https://www.redalyc.org/journal/5055/505565143006/html/

[13] Garcia Leon, R. A.,2015, "Analysis of the behavior of disc brakes in vehicles based on the acceleration of the corrosion process. Tecnura".doi:10.14483/udistrital.jour.tecnura.2015.3.a04

[14] Garcia Leon, R. A.,2020, " Numerical analysis of the thermal behavior of a NACA-type automotive disc brake". INGE CUC. https://revistascientificas.cuc.edu.co/ingecuc/article/view/2301

[15] Garcia Leon, R. A.,2019, "Analysis of air flow in an automotive disc brake with N-38 type ventilation vanes." Scientia et Technica. fhttps://revistas.utp.edu.co/index.php/revistaciencia/article/view/17781fea.

Effect of Nonlinear Thermal Radiation on MHD Flow over a Vertical Cylinder Moving with Nonlinear Velocity

Tarek G Emam*
Department of Mathematics, College of Science and Arts, Khulais, University of Jeddah, Jeddah, Saudi Arabia

ABSTRACT

This paper discusses the effect of nonlinear radiative magnetohydrodynamic flow over a vertical cylinder that moves with nonlinear velocity. The mathematical model of the problem is constructed including different parameters such as the nonlinearity parameter, the thermal radiation parameter, the magnetic parameter, etc. Suitable similarity transformation is used to transform the system of partial differential equations that describes the fluid motion into a system of ordinary differential equations. The obtained system along with the associated boundary conditions is solved numerically using Mathematica. Such method is validated through comparing the results obtained with analytic solutions for some parameter values. Exhibiting the fluid velocity and temperature pro les in graphs enables to understand the effects of different parameters under consideration.

Keywords MHD boundary layer flow, Moving cylinder, Nonlinear thermal radiation, Nonlinear velocity, Similarity solutions

Introduction

Due to the enormous industrial and engineering applications of the flow of Newtonian and Non-Newtonian fluids many authors devoted efforts to such studies, especially in the last few decades. The problem of our concern that is the boundary layer flow over a moving cylinder has many industrial applications such as plastic and metallurgy industries as well as wire drawings. Sakiadis [1] examined the behaviour of boundary layer flow on a moving continuous surface. Rotte and Beek [2] constructed an approximate solution to the case of cooling or heating a continuously moving cylinder. The effects of mass transfer and thermal radiation on the flow of a viscous incompressible fluid past a moving vertical cylinder was analyzed by Ganesan and loganathan [3]. Abo-Eldahab and Salem [4] have recently investigated the problem of flow past a moving cylinder while considering the heat transfer of non-Newtonian power-law fluid with diffusion and chemical reaction. The concept of Magnetohydrodynamic (MHD) arises when we consider the case of fluid flow in electrically conducting fluids whenever magnetic properties affect fluid flow characteristics. A current is induced upon a magnetic field is incident in an electrically conducting fluid. There are enormous industrial applications of MHD in technology such as the industry of Petroleum, plasma studies, designs of MHD power generator, and the design of nuclear reactors. The steady flow of an electrically conducting incompressible fluid past a semi-infinite moving vertical cylinder in the presence of a transverse magnetic field is investigated by Amkadni and Azzouzi [5]. Elbashbesh, et al., [6] presented the study of boundary layer flow over a horizontal stretching cylinder embedded in a porous medium. The study included the effects of thermal radiation, heat transfer, and suction/injection. Abdul Rehman, et al., [7] gave an analytic solution of the flow of a micropolar fluid past over a moving cylinder, in their study they took into consideration axisymmetric stagnation flow. A good view of the electrically conducting boundary layer flow of incompressible viscoelastic nanofluid that flows due to a moving linearly stretching surface can be found in the work of Haroon, et al., [8]. The references [9-15] give a good review for the recent studies of the boundary layer flow over a cylinder. In this paper, we study the problem of heat and mass transfer and MHD flow over a cylinder that moving vertically with nonlinear velocity under the action of a uniform magnetic field, in the presence of nonlinear thermal radiation. An analytic solution will be found for some special cases and numerical solution will be reached and the results will show the effects of different parameters considered here on the fluid velocity and fluid temperature.

Mathematical Model of the Problem

The study assumes an incompressible steady laminar flow over a semi-infinite cylinder of radius R that is moving nonlinearly. The coordinates are designed such that x is measured along the cylinder axis where r intersects with x axis at the origin and refers to the radial coordinate that is normal to the cylinder axis. The fluid properties are considered to be constant. A transverse magnetic field is applied and assumed to be uniform with strength B0 and the external velocity is considered as *ue(x) = u∞(x/l)n, u∞ > 0*. Such assumptions lead to the governing equations:

$$\frac{\partial(rv)}{\partial r}+\frac{\partial(ru)}{\partial x}=0 \tag{2.1}$$

$$u\frac{\partial u}{\partial x}+v\frac{\partial u}{\partial r}=\frac{v}{r}\frac{\partial}{\partial r}(r\frac{\partial u}{\partial r})+u_e\frac{du_e}{dx}+\frac{\sigma B_0^{\,2}}{\rho}(u_e-u) \tag{2.2}$$

$$u\frac{\partial T}{\partial x}+v\frac{\partial T}{\partial r}=\frac{\alpha}{r}[\frac{\partial}{\partial r}(r\frac{\partial T}{\partial r})-\frac{1}{k}\frac{\partial}{\partial r}(rq_r)] \tag{2.3}$$

along with the boundary conditions:

$$\mathrm{u}(\mathrm{R},x)=\mathrm{u}_w(\frac{x}{l})^n, v(R,x)=0, \lim_{r\to\infty}u(r,x)=\mathrm{u}_\infty(\frac{x}{l})^n \tag{2.4}$$

$$T(R,x)=T_w,\ \lim_{r\to\infty}T(r,x)=T_\infty \tag{2.5}$$

Where u and v represent the velocity components along the x and r directions respectively, v stands for the kinematic viscosity, ρ is the density of the fluid, σ is the fluid electrical conductivity, l is taken as the characteristic length, B_0 is the magnetic field intensity, α is the thermal diffusivity, κ is the thermal conductivity, and $q_r=\frac{-4\alpha^*}{3k^*}\frac{\partial T^4}{\partial r}$ is the radiation heat flux in the radial direction, σ^* is the Stefan-Boltzmann constant and k^* is the Rosseland radiation absorptivity.

A stream function ψ is defined as:

$$ru = \frac{\partial \Psi}{\partial r}, rv = -\frac{\partial \Psi}{\partial x} \tag{2.6}$$

Where,

$$\Psi = \sqrt{\frac{vR(n+1)u_\infty}{2}(\frac{x}{l})^{n+1} Rf(\eta)}, \quad \eta = \sqrt{\frac{u_\infty}{2vR(n+1)}(\frac{x}{l})^{n-1}\frac{1}{R}(r^2 - R^2)} \tag{2.7}$$

Where f is the dimensionless stream function and η is the dimensionless similarity variable. Defining the dimensionless temperature as:

$$\theta(\eta) = \frac{T - T_\infty}{T_w - T_\infty} \tag{2.8}$$

The governing equations and boundary conditions thus take the form:

$$\frac{2}{n+1}(\eta K + 1) f''' + (\frac{2K}{n+1} + \frac{\varepsilon(n+1)}{2} f) f'' + n\varepsilon(1 - (f')^2) - M(f' - 1) = 0 \tag{2.9}$$

$$\frac{\in (n+1)^2 P_r}{4K} f\theta' + (1 + R_d(1 + (\theta_w - 1)\theta)^3)\theta' + (\{1 + \mathrm{R}_d(1 + (\theta_w - 1)\theta^3\}C\theta')' = 0 \tag{2.10}$$

Where $K = \sqrt{\frac{2v(n+1)}{u_\infty R}(\frac{l}{x})^{n-1}}$, $\in = \frac{R}{l}$, the magnetic parameter $M = \frac{\sigma B_0^2 R}{\rho u_\infty}(\frac{l}{x})^{n-1}$, P_r is the Prandtl number, the thermal radiation parameter $R_d = \frac{16\sigma^8 T_\infty^3}{3K^8 \kappa}, \theta_w = \frac{T_w}{T_\infty}, C = \frac{r^2}{MR^2}$. The boundary conditions take the form

$$f(0) = 0, f'(0) = \frac{u_w}{u_\infty} = a, f'(\infty) = 1, \theta(0) = 1, \theta(\infty) = 0$$

To solve the system (9)-(11) numerically we transform it into a system of first order ordinary differential equations as follows: $y_1(\eta) = f(\eta)$, $y_2(\eta) = f'(\eta)$, $y_3(\eta) = f''(\eta)$, $y_4(\eta) = \vartheta(\eta)$, $y_5(\eta) = \vartheta'(\eta)$ to get the system

$$y_1' = y_2 \tag{2.12}$$

$$y_2' = y_3 \frac{2}{n+1}(\eta K + 1) y_3' = -(\frac{2K}{n+1} + \frac{\varepsilon(n+1)}{2} y_1) y_3 - \eta \in (1 - y_2{}^2) + M(y_2 - 1) \tag{2.13}$$

$$y_4' = y_5 \tag{2.14}$$

$$(\{1 + R_d(1 + (\theta_w - 1)y_4{}^3\}Cy_5)' = -(1 + R_d(1 + (\theta_w - 1)y_4{}^3)y_5 - \frac{\in (n+1)^2 \mathrm{P_r}}{4K} y_1 y_5 \tag{2.15}$$

subject to the initial conditions:

$$y_1(0) = 0, \ y_2(0) = a, \ y_3(0) = \mathrm{s}, \ \mathrm{y}_4(0) = 1, \ y_5(0) = u \tag{2.16}$$

The numerical values of the parameters are chosen in a suitable way. The values of s and u are priori unknown and are determined as a part of the solution. While the parameters numerical values are assigned according to the problem physics.

Method of Solutions

The mathematical model of the problem is solved numerically using MATHEMATICA through defining a function *F* [*s_,u_*]:= *NDSolve* [12-17]. The numerical values of *s* and *u* are determined through solving the equations $y_2(\eta_m ax) = 1, y_4(\eta_m ax) = 0$. A reasonable start value is assigned to $\eta_m ax$ and hence increased till we nd $\eta_m ax$ for which the difference between two successive values of *s* and those of *u* are less than 10^7. Once ($\eta_m ax$) *s* and *u* are determined, the problem can be solved easily as an initial value problem using the Mathematica function NDSolve. See references [15] and [16]. To ensure the validity of the numerical method used in this work, consider equation (9) in case of n = 1.

$$(\eta K+1)f'''+(K+\varepsilon f)f''+\varepsilon(1-f'^2)-M(f'-1)=0 \quad (3.1)$$

with the boundary conditions:

$$f(0)=0, f'(0)=\frac{u_w}{u_\infty}=a, f'(\infty)=1 \quad (3.2)$$

Where $K=\sqrt{\frac{4v}{u_\infty R}}$ and $M=\frac{\sigma B^2{}_0 R}{\rho u_\infty}$.

The exact solution given in ref [16] is:

$$f(\eta)=\eta+\frac{(a-1)K}{\varepsilon}(1-e^{\frac{-\epsilon\eta}{K}}) \quad (3.3)$$

Here we give a comparison between the numerical solutions of equations (18) and (19) using the numerical method presented in this work and the exact solutions given by equation (20) for some special cases. Such comparison is elucidated in Table 1 which presents a comparison of $f''(0)$ for $K = 0.3$ and $\epsilon = 1$. Column 4 of Table 1 gives the numerical calculated values of $|f''(0) - 1|$. Exact values should be zeroes as $\eta max \to \infty$. Results shown in Table 1 assure the validity of the numerical method presented in this work.

Results and Discussions

In this section, Solutions of the problem is given for different values of the parameters. We study the variance of the fluid velocity $f'(\eta)$ and the temperature of the fluid $\theta(\eta)$ with the similarity variable η for different reasonable values of the

Table 1: Values of $f''(0)$ where $K = 0.3$, $\epsilon = 1$.

a	Exact Sol. ref [16]	Num. Sol.	Error $/f''(0) - 1/$
1.1	-1/3	-0.3333333	2.2722×10^{-12}
1.3	-1	-1.0000000	1.529×10^{-10}
1.5	-5/3	-1.6666667	4.240×10^{-13}
2	-10/3	-3.3333333	7.450×10^{-12}

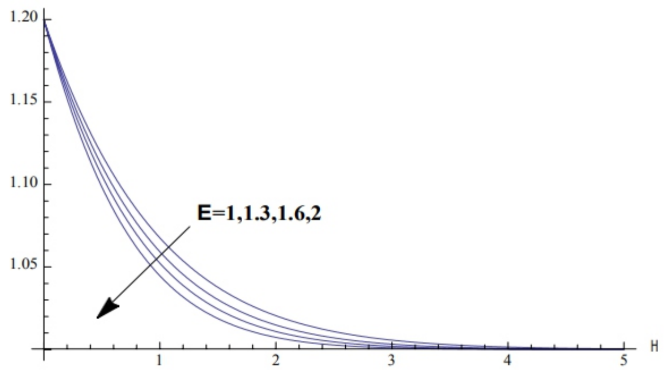

Figure 1: Variation of the fluid velocity $f'(\eta)$ with the parameter ϵ, where $K = 0.2$, $a = 1.2$, $n = 0.3$, $\vartheta_w = 1.1$, $M = 0.4$, $P_r = 7.6$, $R_d = 1$, $C = 2$.

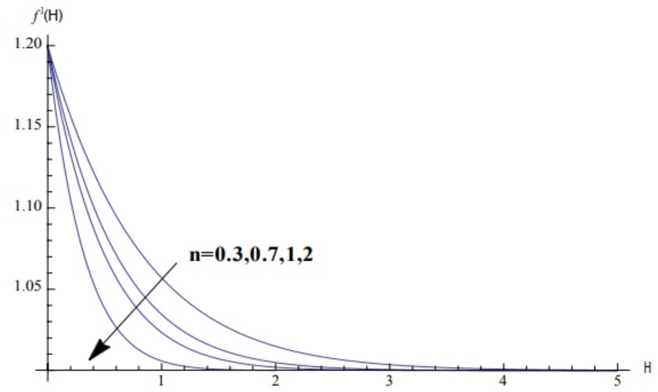

Figure 2: Variation of the fluid velocity $f'(\eta)$ with the parameter n, where $K = 0.2$, $a = 1.2$, $\epsilon = 1$, $\vartheta_w = 2$, $M = 1$, $P_r = 7.6$, $R_d = 1.2$, $C = 2$.

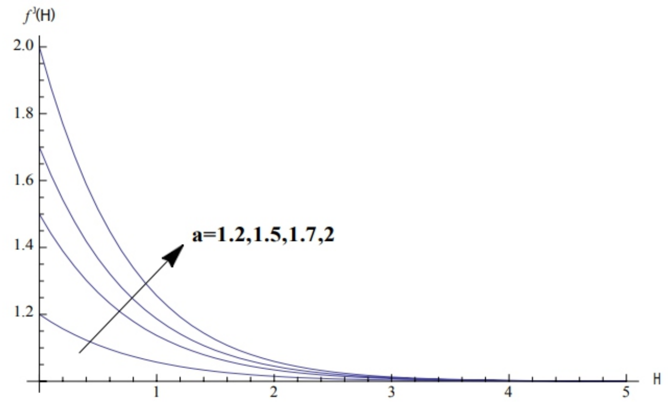

Figure 3: Variation of the fluid velocity $f'(\eta)$ with the parameter a, where $K = 0.2$, $n = 0.3$, $\epsilon = 1$, $\vartheta_w = 2$, $M = 1$, $P_r = 7.6$, $R_d = 1.2$, $C = 2$.

parameters governing the fluid motion. Figure 1, Figure 2, Figure 3, Figure 4, Figure 5 exhibits how the fluid velocity varies with the similarity variable η. The velocity of the fluid changes inversely with η till the velocity becomes one which refers to the case of ambient fluid. Figure 1 shows the fluid velocity is affected by changing the parameter $\in = \frac{R}{l}$. The fluid velocity decreases as ϵ increases. In fact the increase of $\in = \frac{R}{l}$ results in decreasing the cylinder surface area. Shrinking the surface

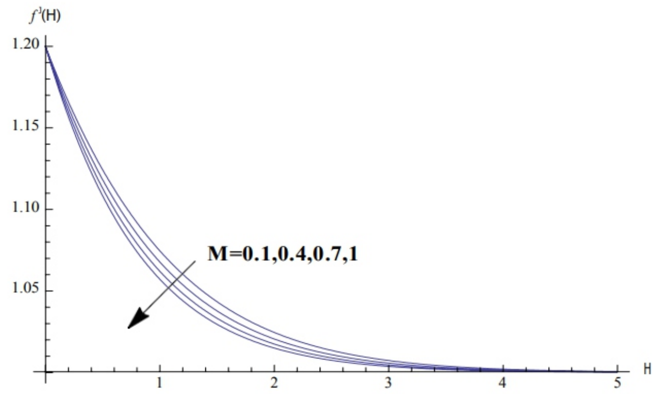

Figure 4: Variation of the fluid velocity $f'(\eta)$ with the parameter M, where $K = 0.2$, $n = 0.3$, $\epsilon = 1$, $\vartheta_w = 2$, $a = 1.2$, $P_r = 7.6$, $R_d = 1.2$, $C = 2$.

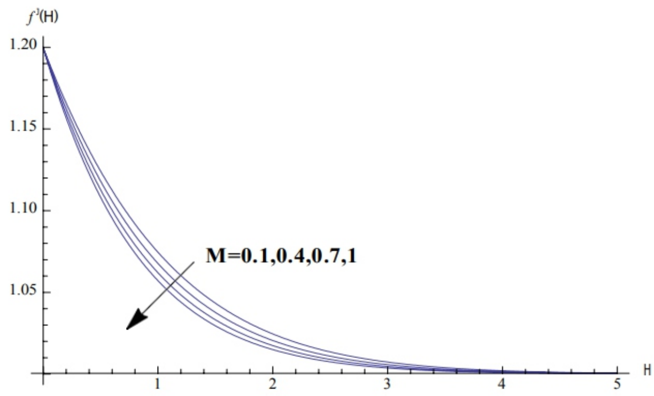

Figure 5: Variation of the fluid velocity $f'(\eta)$ with the parameter K, where $M = 0.4$, $n = 0.3$, $\epsilon = 1$, $\vartheta_w = 1.1$, $P_r = 7.6$, $R_d = 1$, $C = 2$.

area of the cylinder evolves to the increase of the space provided to the free stream velocity which enhances the tendency of the fluid velocity to get the value of the free stream velocity. Figure 2 elucidate the effect of the parameter n on the fluid velocity. The increase of n results in slowing the fluid. Such inverse relation can be understood through investigating the values of $f''(0)$ for different values of n which is shown in Table 2 proving that $f''(0)$ decreases with the increase of n which implies the effect of n on the fluid velocity. The fact that increasing the initial velocity of the fluid gives rise to accelerating the fluid is ensured in Figure 3. The value of $-f''(0)$ and consequently the skin friction coefficient increases as the magnetic parameter M increases as shown in Table 2. Such direct relation enhances the slowing of the fluid as noticed in Figure 4. Figure 5 shows that the fluid velocity decreases with the increase of the value of the parameter K. The justification of this behaviour is that $-f''(0)$ increases with the increase of K as shown in Table 2. The variations of the fluid temperature similarity variable $\theta(\eta)$ that is the difference between the temperature of the fluid and the ambient temperature with η are elucidated in Figures 6, Figure 7, Figure 8, Figure 9, Figure 10, Figure 11, Figure 12. The value of $\theta(\eta)$ decreases as η increases damping to zero which is already expected since as increasing η the fluid temperature gets closer to the ambient temperature value. Figure 6 elucidates the fact that as the initial velocity increases the fluid velocity increases also and consequently the cooling rate evolves which gives rise to decreasing the fluid temperature $\theta(\eta)$. The effect of the variation of the parameter n on the fluid temperature is elucidated in Figure 7. Increasing the value of n results in a decrease of the fluid temperature $\theta(\eta)$ since the increase of n implies an increase of the surface heat ux $-\theta'(0)$ as exhibited in Table 2. Figure 8 exhibits the variation of fluid temperature with the

parameter ϵ. The inverse relation between θ and $\in = \frac{R}{l}$ is a result of the fact that as the cylinder radius increases the cylinder

surface area increases which consequently increases the value of $-\theta'(0)$ and so the fluid temperature decreases. The variation of the Prndtle number has considerable effect on the fluid temperature as shown in Figure 9. Considering the definition of the Prndtle number, one realizes that as Pr increases the fluid thermal conductivity increases which in turn results in increasing the surface heat flux (Table 2) that implies a decrease of the fluid temperature. The thermal radiation parameter affects the fluid temperature as demonstrated in Figure 10. In fact as Rd increases the Rossland radiation absorptivity k* decreases and hence

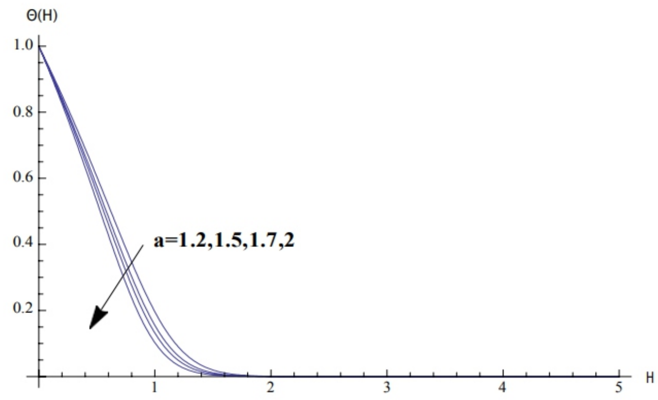

Figure 6: Variation of the velocity $\vartheta(\eta)$ with the parameter a, where $K = 0.2$, $n = 0.3$, $\epsilon = 1$, $\vartheta_w = 2$, $M = 1$, $P_r = 7.6$, $R_d = 1.2$, $C = 2$.

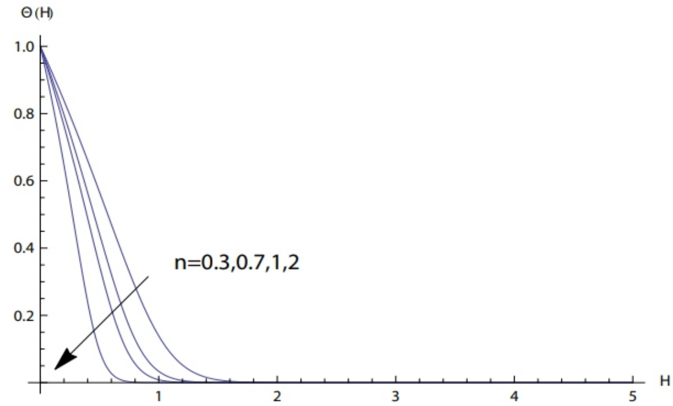

Figure 7: Variation of the fluid velocity $\vartheta(\eta)$ with the parameter n, where $K = 0.2$, $a = 1.2$, $\epsilon = 1$, $\vartheta_w = 2$, $M = 1$, $P_r = 7.6$, $R_d = 1.2$, $C = 2$.

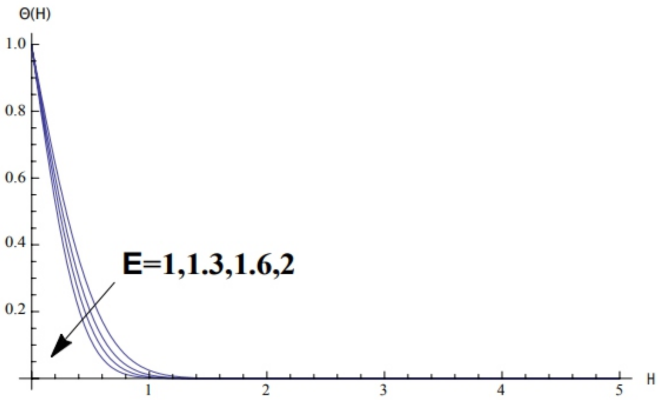

Figure 8: Variation of the fluid velocity $\vartheta(\eta)$ with the parameter ϵ, where $K = 0.2$, $a = 1.2$, $n = 0.3$, $\vartheta_w = 1.1$, $M = 0.4$, $P_r = 7.6$, $R_d = 1.2$, $C = 2$.

the radiation heat flux $q_r = \frac{-4\sigma^*}{3k^*}\frac{\partial T^4}{\partial r}$ increases which leads to an increase of rate of the radiative heat transferred to the fluid which in turn elevates the fluid temperature. From Table 2 one can notice that as the parameter value $\theta_w = \frac{T_w}{T-\infty}$

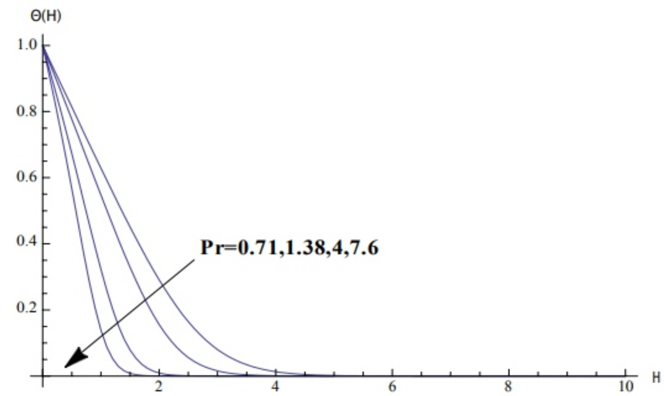

Figure 9: Variation of the fluid velocity $\vartheta(\eta)$ with the parameter P_r, where $K = 0.2$, $a = 1.2$, $n = 0.3$, $\epsilon = 1$, $\vartheta_w = 2$, $M = 1$, $P_r = 7.6$, $R_d = 1.2$, $C = 2$.

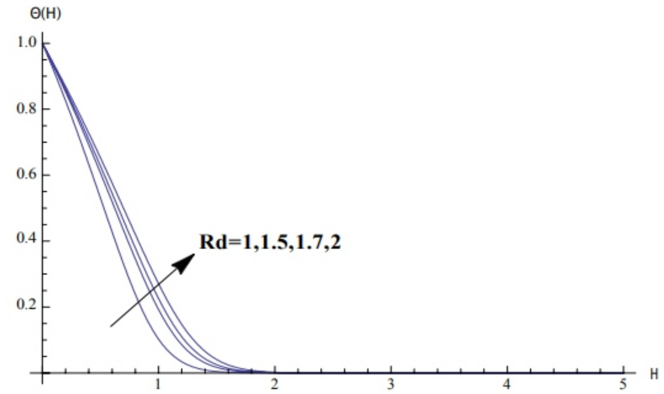

Figure 10: Variation of the fluid velocity $\vartheta(\eta)$ with the parameter R_d, where $K = 0.2$, $a = 1.2$, $n = 0.3$, $\epsilon = 1$, $\vartheta_w = 2$, $M = 1$, $P_r = 7.6$, $C = 2$.

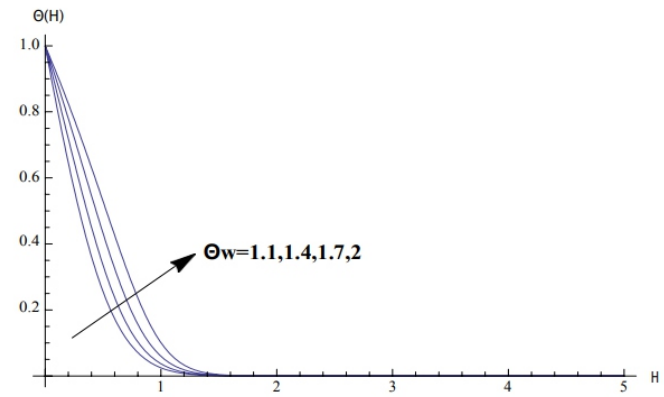

Figure 11: Variation of the fluid velocity $\vartheta(\eta)$ with the parameter ϑ_w, where $K = 0.2$, $a = 1.2$, $n = 0.3$, $\epsilon = 1$, $M = 1$, $P_r = 7.6$, $R_d = 1$, $C = 2$.

increases the wall temperature increases also which gives rise to the enhancement of the fluid temperature as elucidated in Figure 11. The effect of the parameter K on the fluid temperature is shown in Figure 12. The value of $-\theta'(0)$ decreases with the increase of K as elucidated in Table 2. Such variation enforces the fluid temperature to decrease.

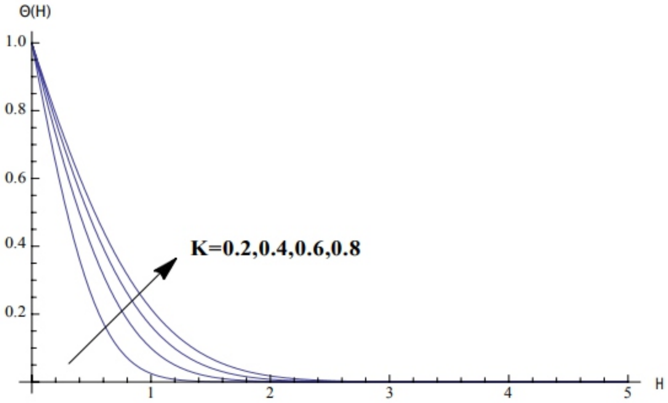

Figure 12: Variation of the fluid velocity $\vartheta(\eta)$ with the parameter K, where $a = 1.2$, $n = 0.3$, $\epsilon = 1$, $\vartheta_w = 1.1$, $M = 0.4$, $P_r = 7.6$, $R_d = 1$, $C = 2$.

Table 2: Values of $-f''(0)$ and $-\theta'(0)$ for various values of the considered parameters.

n	K	ϵ	M	P_r	R_d	ϑ_w	C	A	$-f''(0)$	$-\vartheta'(0)$
0.5	0.4	1.0	1.0	7.6	1.2	2.0	2.0	1.2	0.294076	0.65995
0.7									0.338875	0.717159
0.5									0.405774	0.809287
0.5	0.2	1.0	1.0	7.6	1.2	2.0	2.0	1.2	0.284732	0.852847
	0.4								0.294076	0.655995
	0.6								0.303192	0.570127
0.5	0.4	1.0	1.0	7.6	1.2	2.0	2.0	1.2	0.294076	0.655995
		1.5							0.333143	0.760530
		2.0							0.367911	0.849012
0.5	0.4	1.0	0.4	7.6	1.2	2.0	2.0	1.2	0.259431	0.627275
			0.7						0.277313	0.656602
			1.0						0.294076	0.655995
0.5	0.4	1.0	1.0	0.7	1.2	2.0	2.0	1.2	0.294076	0.342671
				4.0					0.294076	0.528014
				7.6					0.294076	0.655995
0.5	0.4	1.0	1.0	7.6	1.2	2.0	2.0	1.2	0.294076	0.655995
					1.7				0.294076	0.578398
					2.0				0.294076	0.546589
0.5	0.4	1.0	1.0	7.6	1.2	1.4	2.0	1.2	0.294076	1.093853
						1.7			0.294076	0.829356
						2.0			0.294076	0.655995
0.5	0.4	1.0	1.0	7.6	1.2	2.0	2.0	1.2	0.294076	0.655995
							3.0		0.294076	0.504565
							4.0		0.294076	0.420907
0.5	0.4	1.0	1.0	7.6	1.2	2.0	2.0	1.2	0.294076	0.655995
								1.5	0.758729	0.691506
								2.0	1.592643	0.747028

Conclusions

A study of nonlinear radiative flow over a vertical cylinder that moves with nonlinear velocity is given.

The problem is formulated using a suitable mathematical model including all parameters influencing the fluid velocity and temperature. The model is then solved numerically and the numerical results in some special case are compared with exact solutions to assure the validity of the numerical method given in this work. The effects of the parameters are investigated and interpreted physically.

Acknowledgements

This work was funded by the University of Jeddah, Jeddah, Saudi Arabia, under grant No. (UJ-22-DR-50). The authors, therefore, acknowledge with thanks the University of Jeddah for its technical and financial support

References

1. Sakiadis BC (1961) Boundary-layer behavior on continuous solid surfaces: II. The boundary layer on a continuous at surface. AIChE Journal 7: 221-225.

2. Rotte JW, Beek WJ (1969) Some models for the calculation of heat transfer coefficients to a moving continuous cylinder. Chemical Engineering Science 24: 705-716.

3. Ganesan P, Loganathan P (2002) Radiation and mass transfer effects on flow of an incompressible viscous fluid past a moving vertical cylinder. International Journal of Heat and Mass Transfer 45: 4281-4288.

4. Abo-Eldahab EM, Salem AM (2005) MHD Flow and heat transfer of non-Newtonian power-law fluid with diffusion and chemical reaction on a moving cylinder. Heat and Mass Transfer 41: 703-708.

5. Amkadni M, Azzouzi A (2006) On a similarity solution of MHD boundary layer flow over a moving vertical cylinder. Differential Equations and Nonlinear Mechanics 2006: 1-9.

6. Elbashbeshy Elsayed MA, Emam TG, El-Azab MS, et al. (2015) Effect of thermal radiation on flow, heat, and mass transfer of a nanofluid over a stretching horizontal cylinder embedded in a porous medium with suction/injection. Journal of Porous Media 18: 215-229.

7. Rehman A, Iqbal S, Raza SM (2016) Axisymmetric stagnation flow of a micropolar fluid in moving cylinder: An analytical solution. Fluid Mechanics 2: 1-7.

8. Rasheed H, Rehman A, Sheikh N, et al. (2017) MHD boundary layer flow of nanofluid over a continuously moving stretching surface. Applied and Computational Mathematics 6: 265-270.

9. Loganathan1 P, Eswari B (2017) Natural convective flow over moving vertical cylinder with temperature oscillations in the presence of porous medium. Global Journal of Pure and Applied Mathematics 13: 839-855.

10. Manjunatha PT, Gireesha BJ, Prasannakumara BC (2017) Effect of radiation on flow and heat transfer of mhd dusty fluid over a stretching cylinder embedded in a porous medium in presence of heat source. Int J Appl Comput Math 3: 293-310.

12. Matteo DL, Alimhillaj P (2019) Novel fluid dynamic nonlinear numerical models of servo-valves for aerospace. International Journal of Mechanics 13: 39-51.

13. Abdel-Wahed MS, El-Said EM (2019) MHD flow and heat transfer over a moving cylinder in a nanofluid under convective boundary conditions and heat generation. Thermal Science 23: 3785-3796.

14. Mkhatshwa MP, Motsa SS, Ayano MS, et al. (2020) MHD mixed convective nanofluid flow about a vertical slender cylinder using overlapping multi-domain spectral collocation approach. Case Studies in Thermal Engineering 18: 1-12.

15. Elbashbeshy Elsayed MA, Emam TG, El-Azab MS, et al. (2016) Slip effects on flow heat and mass transfer of nanofluid over stretching horizontal cylinder in the presence of suction/injection. Thermal Science 20: 1813-1824.

16. Emam TG (2021) Boundary layer flow over a vertical cylinder embedded in a porous medium moving with nonlinear velocity. WSEAS Transactions in Fluid Mechanics 16: 32-36.

17. Emam TG, Elmaboud YA (2017) Three-dimensional magneto-hydrodynamic flow over an exponentially stretching surface. Int J Heat Technology 35: 987-996.

Instructions for Authors

Essentials for Publishing in this Journal

1 Submitted articles should not have been previously published or be currently under consideration for publication elsewhere.

2 Conference papers may only be submitted if the paper has been completely re-written (taken to mean more than 50%) and the author has cleared any necessary permission with the copyright owner if it has been previously copyrighted.

3 All our articles are refereed through a double-blind process.

4 All authors must declare they have read and agreed to the content of the submitted article and must sign a declaration correspond to the originality of the article.

Submission Process

All articles for this journal must be submitted using our online submissions system. http://enrichedpub.com/ . Please use the Submit Your Article link in the Author Service area.

Manuscript Guidelines

The instructions to authors about the article preparation for publication in the Manuscripts are submitted online, through the e-Ur (Electronic editing) system, developed by **Enriched Publications Pvt. Ltd**. The article should contain the abstract with keywords, introduction, body, conclusion, references and the summary in English language (without heading and subheading enumeration). The article length should not exceed 16 pages of A4 paper format.

Title

The title should be informative. It is in both Journal's and author's best interest to use terms suitable. For indexing and word search. If there are no such terms in the title, the author is strongly advised to add a subtitle. The title should be given in English as well. The titles precede the abstract and the summary in an appropriate language.

Letterhead Title

The letterhead title is given at a top of each page for easier identification of article copies in an Electronic form in particular. It contains the author's surname and first name initial .article title, journal title and collation (year, volume, and issue, first and last page). The journal and article titles can be given in a shortened form.

Author's Name

Full name(s) of author(s) should be used. It is advisable to give the middle initial. Names are given in their original form.

Contact Details

The postal address or the e-mail address of the author (usually of the first one if there are more Authors) is given in the footnote at the bottom of the first page.

Type of Articles

Classification of articles is a duty of the editorial staff and is of special importance. Referees and the members of the editorial staff, or section editors, can propose a category, but the editor-in-chief has the sole responsibility for their classification. Journal articles are classified as follows:

Scientific articles:

1. Original scientific paper (giving the previously unpublished results of the author's own research based on management methods).

2. Survey paper (giving an original, detailed and critical view of a research problem or an area to which the author has made a contribution visible through his self-citation);

3. Short or preliminary communication (original management paper of full format but of a smaller extent or of a preliminary character);

4. Scientific critique or forum (discussion on a particular scientific topic, based exclusively on management argumentation) and commentaries. Exceptionally, in particular areas, a scientific paper in the Journal can be in a form of a monograph or a critical edition of scientific data (historical, archival, lexicographic, bibliographic, data survey, etc.) which were unknown or hardly accessible for scientific research.

Professional articles:

1. Professional paper (contribution offering experience useful for improvement of professional practice but not necessarily based on scientific methods);
2. Informative contribution (editorial, commentary, etc.);
3. Review (of a book, software, case study, scientific event, etc.)

Language

The article should be in English. The grammar and style of the article should be of good quality. The systematized text should be without abbreviations (except standard ones). All measurements must be in SI units. The sequence of formulae is denoted in Arabic numerals in parentheses on the right-hand side.

Abstract and Summary

An abstract is a concise informative presentation of the article content for fast and accurate Evaluation of its relevance. It is both in the Editorial Office's and the author's best interest for an abstract to contain terms often used for indexing and article search. The abstract describes the purpose of the study and the methods, outlines the findings and state the conclusions. A 100- to 250- Word abstract should be placed between the title and the keywords with the body text to follow. Besides an abstract are advised to have a summary in English, at the end of the article, after the Reference list. The summary should be structured and long up to 1/10 of the article length (it is more extensive than the abstract).

Keywords

Keywords are terms or phrases showing adequately the article content for indexing and search purposes. They should be allocated heaving in mind widely accepted international sources (index, dictionary or thesaurus), such as the Web of Science keyword list for science in general. The higher their usage frequency is the better. Up to 10 keywords immediately follow the abstract and the summary, in respective languages.

Acknowledgements

The name and the number of the project or programmed within which the article was realized is given in a separate note at the bottom of the first page together with the name of the institution which financially supported the project or programmed.

Tables and Illustrations

All the captions should be in the original language as well as in English, together with the texts in illustrations if possible. Tables are typed in the same style as the text and are denoted by numerals at the top. Photographs and drawings, placed appropriately in the text, should be clear, precise and suitable for reproduction. Drawings should be created in Word or Corel.

Citation in the Text

Citation in the text must be uniform. When citing references in the text, use the reference number set in square brackets from the Reference list at the end of the article.

Footnotes

Footnotes are given at the bottom of the page with the text they refer to. They can contain less relevant details, additional explanations or used sources (e.g. scientific material, manuals). They cannot replace the cited literature.
The article should be accompanied with a cover letter with the information about the author(s): surname, middle initial, first name, and citizen personal number, rank, title, e-mail address, and affiliation address, home address including municipality, phone number in the office and at home (or a mobile phone number). The cover letter should state the type of the article and tell which illustrations are original and which are not.

Note